J. Fluid Mech. (2017), *vol.* 817, *pp.* 217–263. © Cambridge University Press 2017
doi:10.1017/jfm.2017.92

Experiments on localized secondary instability in bypass boundary layer transition

G. Balamurugan[1] **and A. C. Mandal**[1,†]

[1]Department of Aerospace Engineering, Indian Institute of Technology, Kanpur 208016, India

(Received 18 July 2016; revised 9 February 2017; accepted 9 February 2017;
first published online 16 March 2017)

An experimental study on localized secondary instability of unsteady streamwise streaks in bypass boundary layer transition under an elevated level of free-stream turbulence has been carried out mainly using the particle image velocimetry (PIV) technique. Simultaneous orthogonal dual-plane PIV measurements were performed for a concurrent examination of the transitional flow features in both wall-normal and spanwise planes. These quantitative and simultaneous visualizations clearly show the wall-normal view of a low-speed streak undergoing sinuous/varicose motion in the spanwise plane. An oscillating shear layer in the wall-normal plane is found to be associated with the sinuous/varicose streak oscillation in the spanwise plane. Further, these measurements indicate that a localized secondary instability wavepacket can originate near the boundary layer edge. The time-resolved PIV measurements in the wall-normal plane clearly show how an instability develops on a lifted-up inclined shear layer and leads to flow breakdown. The estimated wavelength and convection velocity of such instabilities are found to compare well with those calculated from the one-dimensional linear stability analysis of the spatially averaged velocity profiles associated with the lifted-up shear layers. The time-resolved PIV measurements in the spanwise plane also facilitate quantitative visualizations of sinuous and varicose instabilities. These measurements experimentally confirm that a varicose instability at the juncture of an incoming high-speed streak and a downstream low-speed streak can eventually lead to the formation of lambda structures. The estimated convection velocity, wavelength and growth rate of these instabilities are found to be consistent with the numerical results reported in the literature. Moreover, the streak secondary instability is found to be apparent in the velocity contours, while the estimated streak amplitude is approximately 30 % of the free-stream velocity.

Key words: boundary layer receptivity, boundary layer stability, transition to turbulence

1. Introduction

Laminar–turbulent transition in a boundary layer has continued to be a potential area of research for decades because of its importance in fundamental and applied aspects of fluid mechanics (e.g. Kachanov 1994). Boundary layer transition over a smooth surface in a zero-pressure-gradient flow is generally distinguished as natural or bypass transition depending on the level of turbulence in the free-stream flow. Natural

---

† Email address for correspondence: alakeshm@iitk.ac.in

transition which occurs at very low levels of free-stream turbulence is characterized by exponential amplification of two-dimensional Tollmien–Schlichting (TS) waves followed by three-dimensional secondary instability and nonlinear breakdown to turbulence (e.g. Kachanov 1994; Reed, Saric & Arnal 1996). On the other hand, bypass transition which occurs at an elevated level of free-stream turbulence (Morkovin 1969) is characterized by the generation of low- and high-velocity streaks followed by their eventual breakdown to turbulent flow (e.g. Kendall 1998; Jacobs & Durbin 2001; Matsubara & Alfredsson 2001). In contrast to TS waves, these streaks grow algebraically at the initial stage of bypass transition (e.g. Kendall 1998; Matsubara & Alfredsson 2001; Fransson, Matsubara & Alfredsson 2005).

The experimental work of Klebanoff (1971) first indicated the existence of low- and high-velocity streaks in a boundary layer under large free-stream turbulence, although he called them ‘breathing modes’. In his experimental work, Kendall (1985) visualized these streaks and named them as ‘Klebanoff modes’. Various authors have contributed to the understanding of the generation of longitudinal streaks and their inviscid/viscous amplification with time, which is found to be algebraic/transient in nature (Ellingsen & Palm 1975; Landahl 1980; Hultgren & Gustavsson 1981). Similarly, the optimal perturbation theory in the boundary layer also reveals spatial transient growth of three-dimensional disturbances (Andersson, Berggren & Henningson 1999; Luchini 2000). The transient growth is due to the non-normal nature of the stability operator which provides non-orthogonal eigenfunctions leading to algebraic growth.

In their theoretical analysis, Goldstein & Wundrow (1998) also found that, for small distortion in the incoming flow over a plate, the stretched vortex lines around the plate leading edge produce streamwise vorticity and velocity perturbation in the boundary layer, which can be related to the generation of the Klebanoff modes in the boundary layer. Using a single wire perpendicular to the free-stream flow and to the plate leading edge, Watmuff and co-workers (Watmuff 2006; Pook & Watmuff 2014) experimentally and numerically demonstrated that the boundary layer is more receptive to the streamwise vorticity than the normal vorticity. In these works, the streamwise vorticity generated through stretching and tilting of the normal vorticity in the contraction plays an important role in generating the Klebanoff streaks in the boundary layer. Leib, Wundrow & Goldstein (1999) reported that the Klebanoff type disturbances in the boundary layer are governed by the linearized unsteady boundary-region equation. Using the interaction of the continuous Orr–Sommerfeld and Squire modes, Zaki & Durbin (2005) also described the generation of boundary layer streaks and their breakdown to turbulent flow.

However, the measured data from various experimental works indicate that the disturbance growth in a boundary layer under large free-stream turbulence is algebraic in nature (e.g. Westin *et al.* 1994; Kendall 1998; Fransson *et al.* 2005). Comparing their data with other experimental data in the literature, Westin *et al.* (1994) found that the disturbance grows as $x^{1/2}$, where x is the streamwise distance. However, they found different proportionality constants for different data. Similarly, Matsubara & Alfredsson (2001) found that the disturbance energy grows linearly with x, and the wall-normal distribution of their measured u_{rms} data compares well with the non-modal theory of Luchini (2000); here, u_{rms} is the root mean squared value of the streamwise fluctuating velocity u. However, Fransson *et al.* (2005) found that the initial disturbance energy varies directly as the square of the free-stream turbulence intensity, Tu^2. Furthermore, they showed that the growth of the disturbance energy (u_{rms}^2/U_0^2, measured at $y/\delta^* = 1.4$) for different turbulent intensities can be collapsed to a single line, while the Reynolds number based on the streamwise distance is scaled with the Reynolds number considered at the position where the u_{rms} value is 10 % of the free-stream velocity, U_0; here y denotes the wall-normal distance and δ^* is the theoretical Blasius displacement thickness.

Several direct numerical simulations (DNS) (e.g. Rai & Moin 1993; Jacobs & Durbin 2001; Brandt, Schlatter & Henningson 2004; Ovchinnikov, Choudhari & Piomelli 2008) on bypass boundary layer transition have recently been carried out with the aim of understanding this transition process in detail. The first DNS on bypass transition by Rai & Moin (1993) did not produce the expected results perhaps because of the problems that existed due to streamwise resolutions (Jacobs & Durbin 2001). However, Jacobs & Durbin (2001) found that their simulation on a boundary layer subjected to large free-stream turbulence provided a good overall agreement with the experiments of Roach & Brierly (1992). In their simulation, they found that instability always sets in in a low-speed streak, and the interaction between the lifted low-speed streak and the free-stream turbulence is the precursor of streak secondary instabilities. On the other hand, the simulation of Brandt *et al.* (2004) suggested that the flow breakdown occurs through the sinuous- and varicose-like streak oscillations, and the varicose-like breakdown appears to be similar to the breakdown feature reported by Jacobs & Durbin (2001). Some of the flow features seen in these simulations have also been experimentally verified using particle image velocimetry (PIV) measurements in bypass transition (Mandal, Venkatakrishnan & Dey 2010; Nolan, Walsh & McEligot 2010). Considering two different length scales at a fixed free-stream turbulence intensity (6 %), Ovchinnikov *et al.* (2008) found that the streamwise streaks are involved in transition for the smaller length scale, whereas the transition mechanism for the larger length scale is different.

While the hotwire measurements of Matsubara & Alfredsson (2001) confirm that the disturbance growth and its wall-normal distribution follow the non-modal theory, their flow visualizations of a streaky boundary layer also reveal that these streaks develop streamwise waviness before they eventually break down to turbulent spots. Similarly, using dye-flow visualizations in bypass transition in a water channel, Mans *et al.* (2005) investigated the natural unforced secondary instability modes, i.e. sinuous and varicose modes located on a low-speed streak. In their later PIV experiment (Mans, de Lange & van Steenhoven 2007), which was confined to the spanwise plane only, they observed the bypass transitional flow features while moving their camera with a speed equal to the average fluid velocity at the measurement plane. Identifying different streak configurations that lead to sinuous instability, they reported the wavenumber and the temporal growth rate of the sinuous instability.

For better understanding, controlled numerical and experimental studies of streak secondary instability in a zero-pressure-gradient boundary layer have been carried out by several authors (e.g. Andersson *et al.* 2001; Asai, Minagawa & Nishioka 2002; Chernoray *et al.* 2006; Vaughan & Zaki 2011). In their controlled experiment, Asai *et al.* (2002) found that the Kelvin–Helmholtz instability of the wall-normal inflectional velocity profile governs the growth of a symmetric varicose mode, whereas a wake type instability of the spanwise velocity profile across the streak governs the growth of an anti-symmetric sinuous mode. Apart from the spatial growth rate, they can predict the most amplified frequency and the wavenumber using the linear stability analysis of the measured mean velocity profiles. Using the inviscid linear stability analysis of a steady base flow and the DNS methods for nonlinear evolution, Andersson *et al.* (2001) found that the streak secondary instability is initially of sinuous type. According to their results, the secondary instability sets in when the critical amplitude of streaks goes beyond 26 %, and the sinuous mode is more unstable than the varicose mode. Considering an unsteady base flow that incorporates the nonlinear development of streaks and mean flow distortion, Vaughan & Zaki (2011) identified the two most unstable modes, which they classified as inner and outer modes. Their instability analysis of the outer mode extends the results of Andersson *et al.* (2001) to unsteady base streaks, and the outer mode becomes unstable while the streak amplitude goes beyond 17 %.

Since the base flows considered in the secondary instability analyses of Andersson *et al.* (2001) and Vaughan & Zaki (2011) are periodic in the spanwise direction, their stability results provide collective instability of the entire row of streaks (Hack & Zaki 2014). However, the secondary instability of the boundary layer streaks is often found to be localized in nature. Considering a realistic base flow from their DNS simulation of bypass transition, Hack & Zaki (2014) carried out stability analysis to characterize the localized secondary instability. Using their two-dimensional linear stability analyses on the cross-sectional velocity field, they found that the calculated temporal growth rate compares with the spatio-temporal growth rate obtained from their DNS data. Their analyses also reveal that the streak amplitude between 20 % and 35 % of the free-stream velocity can lead to a positive growth rate. They also pointed out that the linear stability analysis of realistic flow fields can be useful in various scenarios; for example, the linear stability analysis can be applied to the two-dimensional velocity fields measured by the PIV technique.

Various numerical works indicate that the instability in the boundary layer streaks is excited due to the interaction of the free-stream turbulence with the boundary layer streaks (e.g. Jacobs & Durbin 2001; Durbin & Wu 2007). Schlatter *et al.* (2008) also reported that the localized secondary instability wavepackets in bypass transition are perhaps triggered by the localized free-stream perturbations. Some theoretical and experimental works have also been carried out to understand this viewpoint. Using numerical and asymptotic analyses of the linear perturbation equation, Zaki & Saha (2009) found that the penetration of the vortical disturbance inside the boundary layer increases with viscosity and remains limited with the shear for a single fluid case that they studied. Hernon, Walsh & Mceligot (2007) carried out hotwire measurements in bypass transition, and found that the penetration depth of the free-stream turbulence increases with increasing free-stream turbulent intensities and length scales. On the other hand, a recent experimental study on bypass transition by Nolan & Walsh (2012) revealed that the boundary layer is receptive to the free-stream turbulence only after the occurrence of secondary instability, and the role of the free-stream turbulence is likely to sustain the growth of a turbulent spot after the onset of transition. This observation initiated a new debate which needs further attention.

Some studies on bypass transition point out that the use of only two-dimensional plan views cannot provide all the flow features to understand the associated instability and flow breakdown, and sometimes such an approach can be misleading (Durbin & Wu 2007; Schlatter *et al.* 2008). For example, using the bypass transition model of Zaki & Durbin (2005), the numerical simulation of Schlatter *et al.* (2008) reveals that while the data for both of the planes are simultaneously analysed, the Kelvin–Helmholtz type instability, as was suggested by Jacobs & Durbin (2001) and Zaki & Durbin (2005) from their analyses of the wall-normal plane data, shows its intricate origin in the sinuous streak instability in the spanwise plane. While this contrasting viewpoint certainly invites experimental verification, there exists a difficulty as the instability events in bypass transition under an elevated level of free-stream turbulence occur randomly in space and time. Hack & Zaki (2014) also pointed out that some flow configurations, which are numerically possible and can provide unique knowledge of the transition process, are perhaps difficult or impossible to set up experimentally.

Nonetheless, using three different PIV configurations, an effort has been made to identify and characterize the natural unforced secondary instability events in bypass transition under an elevated level of free-stream turbulence. To examine the flow features of these instability events simultaneously in both the wall-normal and spanwise planes, the simultaneous orthogonal dual-plane PIV technique (Ganapathisubramani *et al.* 2005; Hambleton, Hutchins & Marusic 2006) has been utilized in this work. For further quantitative assessment of their origin, development and breakdown, along with the role of streak amplitude, time-resolved and conventional PIV measurements are separately carried out in the wall-normal and spanwise planes.

This paper is organized as follows. Details of the experimental set-up, measurement techniques and the free-stream turbulence characteristics are described in § 2. The mean flow characteristics are presented in § 3. The results of the simultaneous PIV measurements are discussed in § 4, and the results of the time-resolved PIV measurements are discussed in § 5. The streak amplitude and its relation with the streak secondary instability are discussed in § 6. A summary of the present work, followed by a concluding remark, is presented in § 7.

2. Experimental details

2.1. *Wind tunnel*

The experiments reported in this paper were carried out in a suction type low-turbulence wind tunnel. It is an open-circuit tunnel, which has a 3000 mm long test section with a square cross-section of 610 mm × 610 mm. The settling chamber of the tunnel houses a honeycomb and six screens. The contraction ratio of the tunnel contraction section, which ensures a monotonic velocity increase, is 16:1. The test section of the tunnel was made optically transparent for PIV measurements. The test section is followed by a diffuser of length 3000 mm. The tunnel fan at the diffuser end is driven by an AC motor (14.5 kW), which is controlled by a speed controller. The streamwise turbulence level at the test section, measured following Mandal *et al.* (2010), is found to be 0.1 % of the free-stream velocity, U_0.

Boundary layer measurements were carried out on a transparent acrylic flat plate that was 12 mm thick, 1200 mm long and 610 mm wide. It was mounted horizontally at the midplane of the test section. The plate had an asymmetrical modified superelliptic leading edge, which was designed based on the guidelines suggested by Hanson, Buckley & Lavoie (2012) with a thickness ratio of 7/24 between the working and non-working sides. The leading edge was 120 mm long with aspect ratios of 34.3 and 14.1 for the upper and lower ellipses respectively. Hanson *et al.* (2012) pointed out that a leading edge of this kind reduces the receptivity of the boundary layer by eliminating the discontinuity at the juncture where the curved surface meets the flat surface of the plate. The curvature discontinuity at the juncture can affect the stability properties of the flow (e.g. Saric, Reed & Kerschen 2002). Flat plates with asymmetric leading edges were also utilized in earlier transition studies to reduce the leading edge pressure gradient region (e.g. Klingmann *et al.* 1993; Fransson *et al.* 2005; Li & Gaster 2006). Moreover, a trailing edge flap was used to minimize the leading edge suction peak by positioning the stagnation point along the measurement side of the plate.

2.2. *Measurement techniques: PIV and hotwire anemometry*

We utilized three different PIV configurations, namely the conventional PIV technique, the time-resolved PIV (TR-PIV) technique and the simultaneous orthogonal dual-plane

PIV technique, for this experimental work. All of the PIV measurements in the wall-normal (x–y) plane were carried out at the plate centreline, i.e. $z=0$, and measurements in the spanwise (x–z) plane were carried out at $y=2.5$ mm unless otherwise stated. Here, the streamwise, wall-normal and spanwise directions are denoted by x, y and z respectively. The plate leading edge is at $x=0$, and $y=0$ refers to the wall.

The conventional PIV measurements were carried out using high-resolution CCD cameras (12bit, 8MP Imprex, 10 Hz; 16MP TSI, 2 Hz; 29MP Imperx, 2 Hz) and a Nd:YAG laser (Innolas Spitlight Compact 400 PIV, 180 mJ pulse^{-1}, 10 Hz). The PIV data over a large field of view in bypass boundary layer transition were acquired at a frequency of 2 Hz using the 29MP CCD camera. The measurements in the x–y plane were carried out by centring the camera at $x=303$ mm and 542 mm. The field of view for both of these measurements was $\Delta x\times\Delta y\approx 255$ mm $\times$ 170 mm. Hence, the streamwise distance of a particular PIV measurement zone varied from $(x_c-\Delta x/2)$ mm to $(x_c+\Delta x/2)$ mm, where x_c is the location of the camera centre. The measurements in the x–z plane were carried out in two separate fields of view, i.e. $\Delta x\times\Delta z\approx 272$ mm $\times$ 181 mm and $\Delta x\times\Delta z\approx 308$ mm $\times$ 205 mm, centring the camera at $x=300$ mm and 600 mm respectively. The results of the conventional PIV measurements in bypass boundary layer transition in the x–y and x–z planes are reported in §§ 3 and 6 respectively. The conventional PIV measurements in the Blasius boundary layer, i.e. without using any grid in the test section, and in the free stream, ahead of the plate leading edge, were carried out using the 8MP and 16MP CCD cameras respectively. The fields of view for these measurements were $\Delta x\times\Delta y\approx$ 100 mm $\times$ 75 mm and 107 mm $\times$ 71 mm respectively. These measurements were performed for determination of the virtual origin of the flat-plate boundary layer and for characterization of the grid turbulence respectively.

The TR-PIV measurements were carried out using a high-frequency and high-resolution CMOS camera (resolution: normal mode, 2336 × 1728 pixels; U-mode, 2560 × 1920 pixels; IDTpiv, USA, Model Y5.2) and a high-repetition-rate Nd:YLF DPSS laser (Dual head, 30 mJ pulse^{-1}, 1 kHz, Photonics Industries, USA). The camera could capture 730 images per second (i.e. 365 image pairs per second) at full resolution. However, the frame rate could be increased by reducing the active pixels of the sensor. Utilizing the 2560 pixel × 1080 pixel array of the CMOS camera, all of the TR-PIV data reported here were acquired at 645 Hz (i.e. 1290 images per second). All of the TR-PIV measurements in the x–y and x–z planes were carried out by centring the camera at $x=700$ mm. The fields of view in the x–y and x–z planes were $\Delta x\times\Delta y\approx 104$ mm $\times$ 44 mm and $\Delta x\times\Delta z\approx 140$ mm $\times$ 57 mm respectively, except in § 5.1.2. The field of view of the TR-PIV measurements presented in § 5.1.2 was reduced to $\Delta x\times\Delta y\approx$ 66 mm $\times$ 28 mm for better spatial resolution in the wall-normal plane.

The simultaneous orthogonal dual-plane PIV measurements were carried out following the works of Ganapathisubramani *et al.* (2005) and Hambleton *et al.* (2006), who used this technique for measurements in a turbulent boundary layer. This technique is based on the polarization characteristics of scatted light from seeding particles (see Kähler & Kompenhans 2000, for details). Using this measurement technique, the conventional PIV measurements were carried out in the x–y and x–z planes simultaneously. Figure 1 shows the present measurement set-up schematically. The x–y plane at $z=0$ was illuminated using a Quantel Evergreen Nd:YAG double pulsed laser with an energy of 200 mJ per pulse. The laser beam had been passed through a half-wave plate before it entered into the sheet forming optics. The

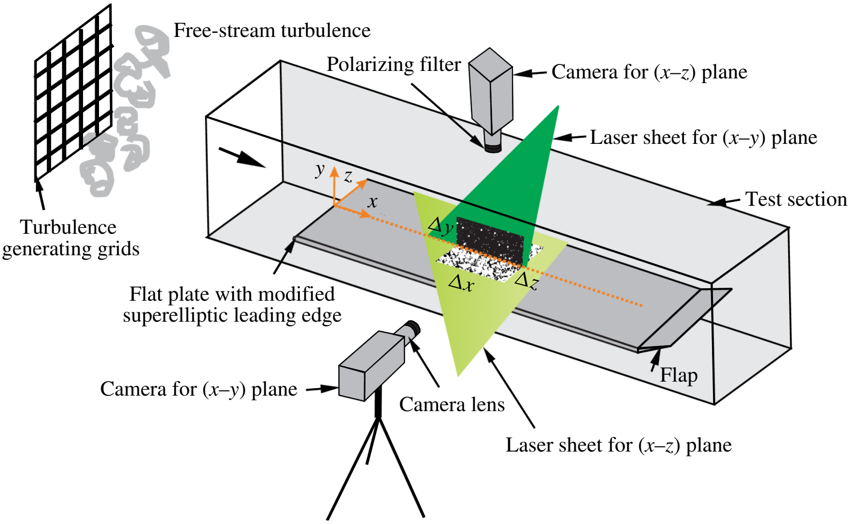

FIGURE 1. (Colour online) A schematic of the simultaneous orthogonal dual-plane PIV measurement set-up in the wind tunnel test section.

half-wave plate rotated the polarization of the beam by 90°. Thus, the initial laser beam, which was vertically polarized, was changed to a horizontally polarized laser beam. On the other hand, the x–z plane at $y = 2.5$ mm from the plate surface was illuminated using the Innolas Nd:YAG laser, details of which are given above. In this case, the initial vertical polarization of the laser beam was preserved. The illuminated particles in the x–y plane were imaged by using a 12 bit 1MP PCO pixelfly CCD camera. Two polarizing filters were mounted in front of this camera lens which could be rotated independently to allow only the horizontally polarized light of the wall-normal plane laser and block the vertically polarized light from the wall-parallel plane laser. The flow field in the x–z plane was captured using the CMOS camera, described above, and the two polarizing filters mounted in front of this camera lens were adjusted to allow only the vertically polarized laser light. With these arrangements, major reflections from the plate surface and from the line of intersection of the two perpendicular laser sheets were minimized. Following Hambleton *et al.* (2006), a series of image processing steps were also performed in MATLAB to retain the information at the intersection. Centring the CCD camera at $x = 700$ mm, the simultaneous PIV measurements were carried out at 5 Hz. The fields of view in the x–y and x–z planes were $\Delta x \times \Delta y \approx 46$ mm $\times$ 34 mm and $\Delta x \times \Delta z \approx 57$ mm $\times$ 43 mm respectively. The field of view in the x–y plane was chosen to be smaller for better spatial resolution.

All of the cameras used here were equipped with 100 mm focal length lenses (Carl Zeiss Macro-Planar lenses). The laser and the camera were synchronized using pulse generators (BNC Nucleonics, Model 575, and IDTpiv, Motion Pro Timing hub). The flow was seeded with glycol based fog particles with a mean diameter of approximately 1 μm. These particles were generated using a SAFEX fog generator (Dantec Dynamics, Denmark). The acquired images were processed using the package ProVision XS, IDTpiv, with a correlation window of 32 pixel × 32 pixel. This package is based on the second-order-accurate mesh-free algorithm developed by Lourenco & Krothapalli (2000). This package was also used in our previous work (e.g. Mandal & Dey 2011; Phani Kumar, Mandal & Dey 2015), and more details on the data processing can be found in Mandal *et al.* (2010). However, based on the correlation window, the spatial resolutions of the conventional PIV measurements in bypass boundary layer transition were found to be 1.3 mm and 1.5 mm in the x–y and x–z planes respectively. Similarly, the spatial resolutions of the conventional PIV measurements in the Blasius boundary layer (without using any grid in the test section) and in the free stream (in front of the leading edge) were found to be 0.97 mm and 0.69 mm respectively. The spatial resolutions of the TR-PIV measurements for the two different fields of view in the x–y plane, as mentioned above, were found to be 0.8 mm and 1.3 mm, whereas the spatial resolution in the x–z plane was found to be 1.75 mm. The spatial resolutions for the simultaneous orthogonal PIV measurements in the x–y and x–z planes were found to be 1 mm and 0.7 mm respectively. While these values compare well with published work on boundary layers (e.g. Liu, Adrian & Hanratty 2001; Dennis & Nickels 2011), a high-resolution feature is also in-built in this package; details can be found in the literature (Lourenco & Krothapalli 2000; Alkislar, Krothapalli, & Lourenco 2003). Therefore, the actual spatial resolution of our measurements is expected to be even better than the values mentioned above.

Although the PIV technique is now considered to be a reliable tool for whole-field velocity measurements, one has to consider the uncertainty involved in the measured values. Sources often considered for error/uncertainty analysis are equipment, particle lag, sampling size and the processing algorithm (e.g. Lazar *et al.* 2010). Considering equipment error, sampling size (random error) and the processing algorithm (bias error) in the present PIV measurements, the overall/combined standard uncertainty (Coleman & Steele 2009) was found to be within $\pm 1.3\,\%$ of the free-stream velocity. Uncertainty due to particle lag was neglected as it is often reported to be negligible for glycol based fog particles (e.g. Raghav & Komerath 2014). The error due to the processing algorithm was estimated by generating synthetic particle image pairs with known pixel displacements (Raffel *et al.* 2013).

A constant-temperature hotwire anemometry system (Dantec Dynamics, Denmark) was also utilized for the present experimental work. A single-wire probe (55P11, Dantec Dynamics), which was connected to a multichannel CTA system (54N81), was used for data acquisition. The sensing element of this probe was a 5 μm diameter tungsten wire, and its length to diameter ratio was 250. The data were acquired using a 16 bit National Instruments data acquisition card (NI-6034E) and LabVIEW software. Setting the overheat ratio at 1.8, data were acquired at a sampling rate of 6 kHz and low-pass filtered at 3 kHz. Without installing any grid in the tunnel test section, the hotwire probe was often calibrated using a Pitot-static tube connected to a digital manometer (Furness Controls, FC012), and the King's law fit. The hotwire data were used to characterize the free-stream turbulence and the flow intermittency in the boundary layer. A hotwire probe in the plate centreline was often placed at the end of the PIV measurement region at $y = 2.5$ mm for simultaneous observation and acquisition of the flow signal during PIV measurements. The uncertainty analysis of the hotwire data was carried out following Yavuzkurt (1984), and the overall uncertainty was found to be within $\pm 1.7\,\%$ of the free-stream velocity.

2.3. *Free-stream turbulence characteristics in the test section*

Turbulence generating grids have served as important experimental devices in the study of bypass boundary layer transition, and square mesh grids are often used

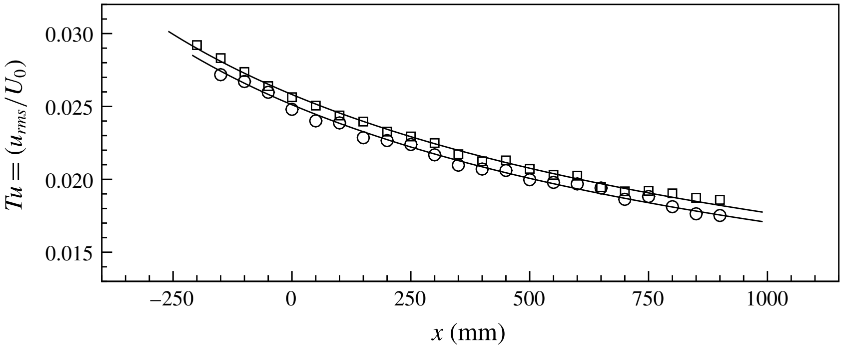

FIGURE 2. Downstream turbulence decay for grids A and B; symbols: ○, grid A; □, grid B. Solid line: curve fitted using (2.1).

to investigate the effect of free-stream turbulence on boundary layer transition (e.g. Westin *et al.* 1994; Matsubara & Alfredsson 2001; Fransson *et al.* 2005; Hernon *et al.* 2007; Nolan *et al.* 2010). However, few works have been carried out using parallel rod/bar grids, mainly focusing on streak generation and their initial development in bypass transition (e.g. Kendall 1985; Roach & Brierly 1992; Pook, Watmuff & Orifici 2016). Here, we intend to focus on the secondary instability characteristics of the boundary layer streaks generated by a parallel rod grid and a square mesh grid, identified as grid A and grid B respectively, to investigate the effect of grid geometry on the streak secondary instability, if any. The parallel rod grid (grid A) was installed in the tunnel such that the bars were perpendicular to the free stream and parallel to the plate leading edge, in contrast to the work of Pook *et al.* (2016) where a screen model made of parallel bars installed in the settling chamber of a wind tunnel was used such that the bars were perpendicular to the free-stream flow and to the plate leading edge.

Grid A was made of uniformly spaced parallel cylindrical rods with a centre-to-centre distance of 34 mm. Grid B was made of cylindrical rods arranged perpendicularly in two different planes so that they formed a square mesh with a mesh width of 44 mm. Both grid A and grid B were made of cylindrical rods of 10 mm diameter. Grid solidity (S_g) is defined as $S_g = 1 - \beta$, where β is the porosity (e.g. Roach 1987; Kurian & Fransson 2009). In terms of the mesh width, M, and the bar/rod diameter, d, the porosity can be expressed as $\beta = (1 - (d/M))$ for a parallel rod grid and $\beta = (1 - (d/M))^2$ for a square mesh grid (e.g. Roach 1987). Using these expressions, the solidities for grids A and B were found to be 0.294 and 0.403 respectively. However, the grids were placed near the entrance of the test section. The distances of grids A and B from the leading edge (x_{grid}) were -1165 mm and -1185 mm respectively. Using the hotwire anemometry technique, the streamwise turbulent intensity, Tu, was measured at various downstream locations to characterize the free-stream turbulence. The measurements were carried out at $U_0 = 5.8$ m s^{-1} and 6.4 m s^{-1} for grids A and B respectively. For both of the grids, the measured data, as shown in figure 2, follow the power-law decay (e.g. Westin *et al.* 1994; Mandal *et al.* 2010) given by

$$Tu = \frac{u_{rms}}{U_0} = C(x - x_{vo})^{-b}, \tag{2.1}$$

where x_{vo} is the virtual origin of a grid, b is the exponential decay rate and C is a constant for a particular grid. The geometric parameters and the numerical values

Grid	Grid type	Bar geometry	Mesh width (mm)	x_{grid} (mm)	S_g	C	x_{vo}	b
Grid A	Parallel rods	Circular	34	−1165	0.294	1.67	−1102	−0.6
Grid B	Square mesh	Circular	44	−1185	0.403	1.76	−1141	−0.6

TABLE 1. Details of grids A and B, and the power-law constants.

of these constants for these grids are given in table 1. The value of b, which is a measure for isotropic turbulence, was found to be 0.6 for both of the grids, and this value compares well with the values reported in the literature (e.g. Westin *et al.* 1994; Fransson *et al.* 2005; Mandal *et al.* 2010). The streamwise turbulent intensities at the plate leading edge were found to be 2.5 % and 2.6 % of the free-stream velocity for grids A and B respectively. The integral length scale, Λ_x, and the Taylor microscale, τ_x, were estimated from the auto-correlation function of the streamwise fluctuating velocity, R_{uu}, at the leading edge (e.g. Mandal *et al.* 2010). The numerical value of the integral length scale was found to be 17 mm, whereas the numerical value of the Taylor microscale was found to be 7(±1) mm, for both of the grids.

For further characterization of the free-stream turbulence, conventional PIV measurements in the x–y and x–z planes were separately carried out in the free-stream flow. Due to experimental constraints in optical access at the leading edge position, the measurements were performed ahead of the plate leading edge, as schematically shown in figure 3(*a*). For measurements in the x–y and x–z planes, the camera was centred at approximately $x = -185$ mm, $y = 100$ mm and $z = 0$ mm, such that the measurement zone was at least 20 mesh widths downstream of the grid location. The measurement field of view (107 mm × 71 mm) and the number of PIV realizations were chosen such that the present spatial resolution, 0.69 mm, and the number of PIV realizations, 1500, were comparable with published PIV measurements on grid generated turbulence (e.g. Gomes-Fernandes, Ganapathisubramani & Vassilicos 2012). Here and in the following, the streamwise, wall-normal and spanwise fluctuating velocities are denoted by $u(= U_I - U)$, $v(= V_I - V)$ and $w(= W_I - W)$ respectively, the local instantaneous velocities in the x-, y- and z-directions are denoted by U_I, V_I and W_I respectively, and the corresponding local mean velocities in these directions are denoted by U, V and W respectively.

For investigation of the longitudinal and transverse length scales associated with an any turbulent velocity fluctuations, q, the two-point spatial correlations

$$R_{qq}(r) = \frac{\overline{q(r_i, t)q(r_i + r, t)}}{\sqrt{\overline{q^2(r_i, t)}}\sqrt{\overline{q^2(r_i + r, t)}}} \tag{2.2}$$

were estimated from the measured data; here, r_i denotes a reference point, with r the separation between two points, and an overbar denotes an ensemble average over the number of PIV realizations. The spatial correlation is called the longitudinal correlation when r is parallel to the direction of q and the transverse correlation when r is perpendicular to the direction of q (O'Neill *et al.* 2004). Measured two-point spatial correlations at $x = -200$ mm are shown in figures 3(*b*) and 3(*c*) for grids A and B respectively. For comparison, the longitudinal, $f(r)$, and transverse, $g(r)$, correlation functions, which are related as

$$f + \frac{1}{2} r \frac{\mathrm{d}f}{\mathrm{d}r} = g \tag{2.3}$$

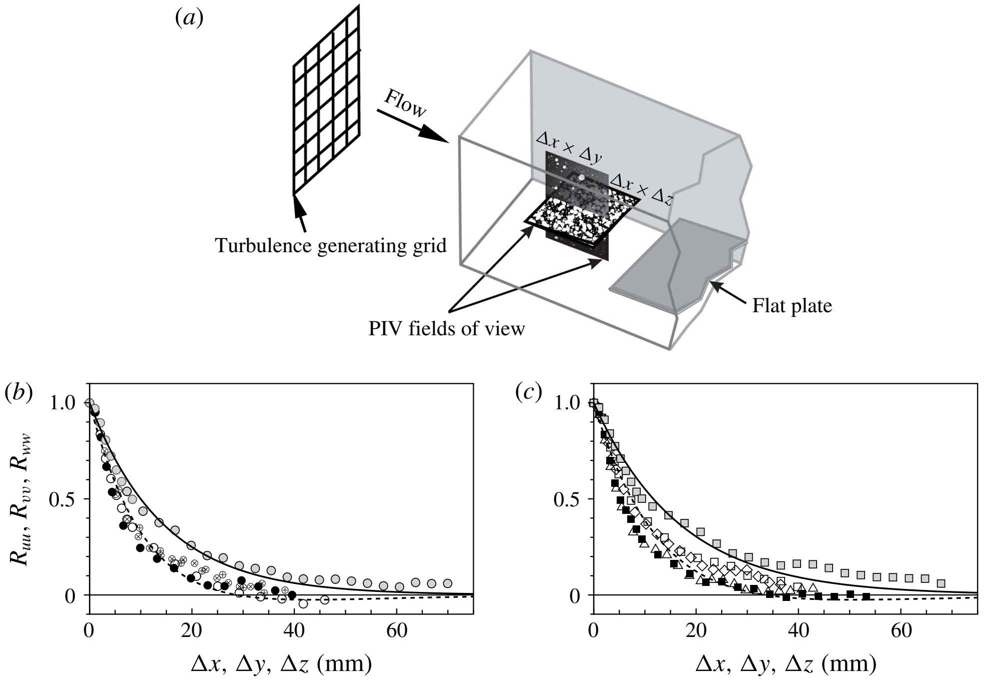

FIGURE 3. Conventional PIV measurements in the free stream for characterization of grid generated turbulence. (*a*) A schematic illustrating the measurement planes. (*b*,*c*) Spatial correlations for grids A and B respectively; longitudinal, *f* (——), and transverse, *g* (- - -), correlation functions calculated from the isotropic relation (2.3) are also plotted for comparison with the measured data. Symbols in (*b*): •, R_{uu} versus Δx; ○, R_{vv} versus Δx; ●, R_{ww} versus Δx; ⊕, R_{uu} versus Δy; ⊗, R_{uu} versus Δz. Symbols in (*c*): ▨, R_{uu} versus Δx; ■, R_{vv} versus Δx; △, R_{ww} versus Δx; □, R_{uu} versus Δy; ◇, R_{uu} versus Δz.

for homogeneous isotropic turbulence (e.g. Batchelor 1982; Kurian & Fransson 2009), are also displayed in figure 3(*b*,*c*). The longitudinal correlation function in homogeneous isotropic turbulence is often approximated as $f(r) = \mathrm{e}^{-r/\varLambda_x}$, where $\varLambda_x$ is the longitudinal integral length scale (e.g. Roach 1987; Kurian & Fransson 2009). We may note that the longitudinal integral length scale, $\varLambda_x$, is estimated from the hotwire data at $x = -200$ mm and $g(r)$ is obtained from (2.3). The present data in figure 3(*b*,*c*) are found to be similar to those reported by Kurian & Fransson (2009). Therefore, the present free-stream turbulence can be considered as nearly isotropic for both of the grids. However, the data for grid A appear to compare better with the calculated $f(r)$ and $g(r)$ functions than the data for grid B. This may be because of the fact that the measurement location is at larger distance in terms of mesh width for grid A than that for grid B, as the mesh width for grid A is less compared with grid B.

The longitudinal ($\varLambda_x$) and transverse ($\varLambda_y$, $\varLambda_z$) integral length scales and the corresponding Taylor microscales (τ_x, τ_y, τ_z) were estimated from the auto-correlation functions of the streamwise velocity fluctuations in the respective directions (e.g. Westin *et al.* 1994; Matsubara & Alfredsson 2001). The transverse integral length scales ($\varLambda_y$, $\varLambda_z$) and the corresponding Taylor microscales (τ_y, τ_z) can also be estimated from the auto-correlation functions of the cross-stream velocity fluctuations in the

Grid	Λ_z (mm)	λ_z (mm)	Λ_y (mm)	λ_y (mm)	Λ_x (mm)	λ_x (mm)
Grid A	9.3 (8.3)	5.4 (5.2)	9.7 (8.4)	5.5 (5.4)	14.4	6.9
Grid B	10.9 (8.8)	5.6 (5)	11.7(8.2)	6.2 (5.3)	16.8	7.4

TABLE 2. Longitudinal and transverse integral and Taylor microscales estimated at $x = -200$ mm; the data inside parentheses refer to the corresponding transverse scales estimated from the auto-correlation functions of the cross-stream velocity fluctuations in the x-direction.

x-direction. The correlation curves were numerically integrated up to the zero-crossing point (e.g. O'Neill *et al.* 2004) to estimate all of the length scales reported here. The estimated length scales at $x = -200$ mm are provided in table 2; it should be noted that the data given inside parentheses refer to the corresponding transverse scales estimated from the auto-correlation functions of the cross-stream velocity fluctuations in the x-direction. We may note that the value of Λ_x in table 2 is estimated from the hotwire data at $x = -200$ mm, as $R_{uu}(\Delta x)$ does not reach zero because of the smaller PIV field of view. The uncertainty in the estimated Taylor microscales is found to be within ±1 mm.

2.4. *Pressure gradient characteristics in the test section*

The streamwise variation of the free-stream pressure coefficient, $C_p = 1 - (U/U_r)^2$, as shown in figure 4, was determined by measuring the local mean velocity in the free stream (e.g. Westin *et al.* 1994; Mandal *et al.* 2010). Here, U_r denotes the reference velocity. The velocity measurements in the free stream were carried out using a hotwire probe, which was first calibrated using a Pitot-static tube without any grid in the test section. Then, the measurements were carried out without installing any grid in the test section for the no-grid case and with the respective grid installed for the grid cases. The probe was kept at $y = 25$ mm from the wall, and it was then traversed along the plate centreline for velocity measurements. The reference point was chosen at $x = 340$ mm for the no-grid case and at approximately $x = 668$ mm for the grid cases. The initial large value of C_p near the leading edge is attributed to the leading edge shape. However, with and without a grid in the test section, the variation of C_p within the domain of our investigation was approximately $\pm 2\,\%$. Similar variation of the pressure coefficient is also reported in various works on bypass transition (e.g. Arnal & Juillen 1978; Roach & Brierly 1992).

3. Mean flow characteristics

Mean flow quantities in the boundary layer are presented mainly to ensure the consistency of our measurements with the published results in the literature. Without installing any turbulence generating grid in the test section, conventional PIV measurements in the x–y plane were carried out to determine the virtual origin of the Blasius boundary layer. Centring the camera at $x = 250$ mm, 450 mm and 650 mm respectively, the PIV measurements were carried out at $U_0 = 4.8$ m s^{-1}. The displacement thickness, δ^*, was estimated from the mean velocity profiles obtained by an ensemble average of 1000 PIV realizations. Following Pook *et al.* (2016), the estimated values of Re_{δ^*} were plotted against $R(=\sqrt{U_0 x/\nu})$, as shown in figure 5, and

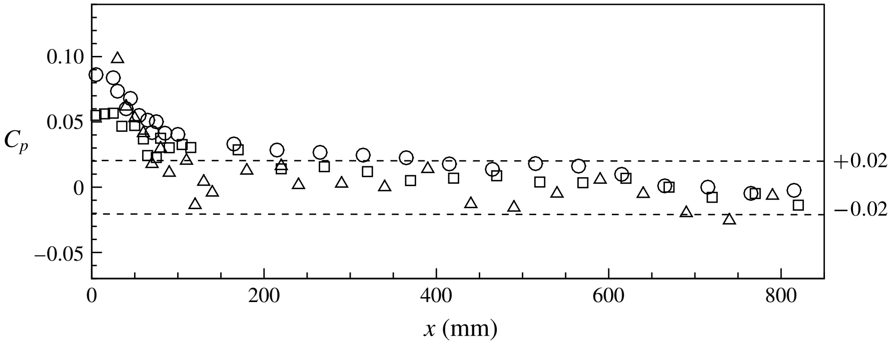

FIGURE 4. Variation of the pressure coefficient, C_p, in the streamwise direction for grids A and B. Data without any grid in the test section are also shown. Symbols: ○, grid A; □, grid B; △, no grid.

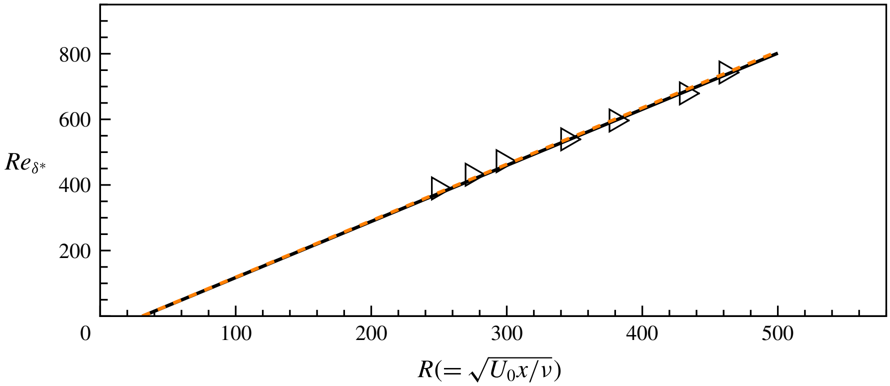

FIGURE 5. (Colour online) Determination of the virtual origin of the Blasius boundary layer without a grid in the tunnel test section. Description of symbols and lines: ▷, measured data; ——, a linear fit to the measured data within $x = 400$ mm–700 mm; - - -, Blasius line from the virtual origin.

a straight line was fitted to find the virtual origin of the boundary layer. It should be noted that the data points within $x = 200$–300 mm were not used in the straight line fitting to avoid the effect of leading edge on the initial boundary layer development (e.g. King 2000). The virtual origin of the boundary layer, x_v, was found to be at $x = 3.1$ mm. Moreover, the Blasius relation, $Re_{\delta^*} = 1.72\sqrt{U_0(x - x_v)/\nu}$, is shown as a dashed line in figure 5 for comparison. As the value of x_v was found to be small, it has not been taken into account while presenting the results.

Boundary layer measurements under a high level of free-stream turbulence were carried out at $U_0 = 4.8$ m s^{-1} and 5.2 m s^{-1} for grids A and B respectively. For these measurements in the x–y plane, the camera was centred at $x = 302$ mm and 542 mm for both of the grids. The boundary layer parameters, i.e. the momentum thickness, θ, the displacement thickness, δ^*, the Reynolds numbers based on δ^*, at the location of the camera centre, x_c, and the number of PIV realizations, N, used for ensemble averaging are given in table 3. The measurement uncertainties of the displacement thickness (δ^*), the momentum thickness (θ) and the Reynolds number (Re_{δ^*}) reported in this paper were found to be within ±2.3 %, ±2.6 % and ±3.5 %

Grid	U_0 (m s^{-1})	x_c (mm)	δ^* (mm)	θ (mm)	Re_{δ^*}	Number of PIV realizations (N)
Grid A	4.8	303	1.8	0.7	559	1050
Grid A	4.8	542	2.4	1.0	745	1050
Grid B	5.2	303	1.7	0.7	556	1050
Grid B	5.2	542	2.3	0.9	753	1050

TABLE 3. Measurement details and boundary layer parameters for grid cases in § 3.

of the estimated values respectively. However, comparison of our measured mean velocity profiles with the Blasius profile in figure 6(a) shows a velocity gain in the lower part of the boundary layer and a velocity deficit in the outer part of the boundary layer. The wall-normal distribution of the u_{rms} profiles in figure 6(b) and the comparison of this wall-normal distribution with the non-modal theory of Luchini (2000) in figure 6(c) are found to be similar to the results reported in the literature (e.g. Westin *et al.* 1994; Matsubara & Alfredsson 2001; Mandal *et al.* 2010). The linear streamwise growth of $(u_{rms,max}/U_0)^2$ is found to collapse for both of the grids, as shown in figure 6(d), when, following Fransson *et al.* (2005), the streamwise Reynolds number, Re_x, is scaled using the Re_x value at $u_{rms,max}/U_0 = 0.1$. We also find that the present data follow the linear fit of Fransson *et al.* (2005), which is reproduced from their paper and shown in figure 6(d), for comparison purposes. The small difference seen in figure 6(d) may be attributed to the receptivity characteristics of the two slightly different leading edges utilized in these two works. However, it is interesting to note that the present PIV measurements and the hotwire measurements of Fransson *et al.* (2005) show almost the same normalized energy growth, although these two measurements were carried out at two different facilities and at different turbulent intensities.

4. Simultaneous orthogonal dual-plane PIV data

Previous experimental studies on bypass transition (e.g. Mans *et al.* 2007; Mandal *et al.* 2010; Nolan & Walsh 2012) have considered PIV realizations in one plane at a time to study the transitional flow features. Since bypass transition under an elevated level of free-stream turbulence is highly unsteady, and three-dimensional in nature, it may be more interesting and revealing to consider instantaneous PIV realizations in both the x–y and x–z planes simultaneously. Such measurements in turbulent boundary layer flows are also found to be fruitful (Ganapathisubramani *et al.* 2005; Hambleton *et al.* 2006).

Centring the camera at $x = 700$ mm, the present simultaneous PIV measurements in the x–y and x–z planes, as detailed in § 2.2, were carried out at $U_0 = 5.8$ m s^{-1} and 6.4 m s^{-1} for grid A and grid B respectively. We may note that these simultaneous measurements, compared with the measurements reported in § 3, were carried out at a higher free-stream velocity and at a further downstream location. This was mainly to ensure that the transitional flow in the boundary layer had developed a certain level of flow intermittency, so that the possibility of imaging instability events was increased in the simultaneous PIV data. To find the flow intermittency, the streamwise velocity data were acquired at $x = 700$ mm and $y = 2.5$ mm using a single hotwire probe. The intermittency, γ, was estimated based on the dual slope method of Kuan & Wang (1990), as detailed in Balamurugan (2014). The numerical values of the

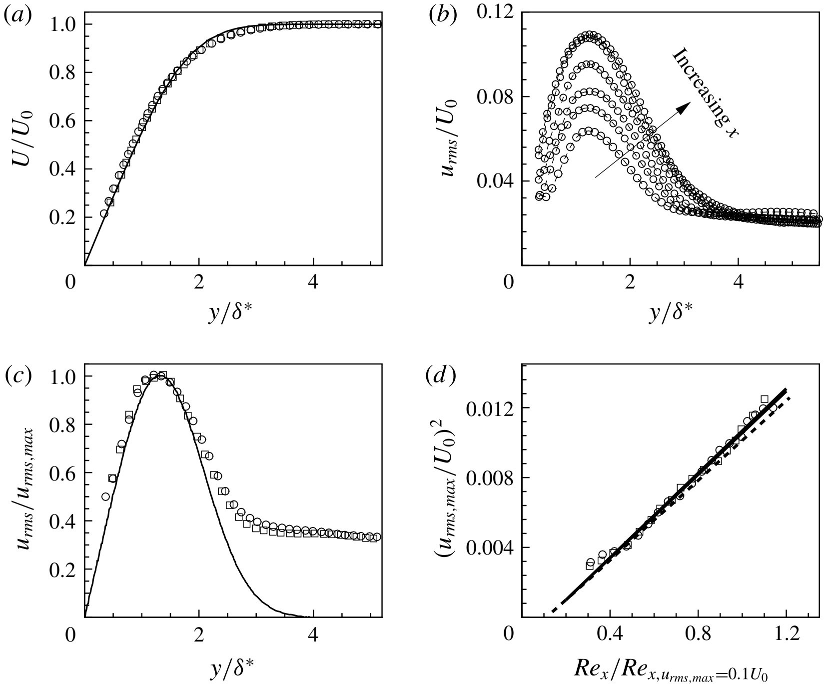

FIGURE 6. Mean flow characteristics for grids A and B. Symbols: ○, grid A; □, grid B. (*a*) Wall-normal variation of the normalized streamwise mean velocity profiles at $x_c = 542$ mm; ——, Blasius profile; data are shown only at one location for clarity. (*b*) Wall-normal distribution of u_{rms}/U_0 at $x = 270$, 334, 392, 509, 617 and 636 mm; the dashed lines with symbols are for clarity only. (*c*) Comparison of the $u_{rms}/u_{rms,max}$ profiles with the optimal disturbance theory of Luchini (2000) at $x_c = 303$ mm; ——, line from figure 6 of Luchini (2000). (*d*) Variation of $u^2_{rms,max}/U^2_0$, with $Re_x/Re_{x,u_{rms,max}=0.1U_0}$; solid lines: linear fit to the present data; - - - -, data reproduced from figure 10(*b*) of Fransson *et al.* (2005), for comparison.

Grid	U_0 (m s^{-1})	x_c (mm)	δ^* (mm)	θ (mm)	Re_{δ^*}	γ (%)	Number of image pairs (N)
Grid A	5.8	700	2.4	1.1	916	5.7	3000
Grid B	6.4	700	2.2	1.0	918	7.3	2250

TABLE 4. Measurement details and boundary layer parameters of the simultaneous PIV data, where x_c is the centre of the measurement region.

flow intermittency at the above mentioned velocities are given in table 4, for both of the grids. Further details of the simultaneous measurements, i.e. the boundary layer parameters and the number of simultaneous PIV realizations, are also provided in table 4. In the following, the displacement thickness (δ^*) and the free-stream velocity (U_0) corresponding to a particular grid, as mentioned in table 4, are used as the length and velocity scales for normalization, unless otherwise stated. Moreover, a new variable, x_1, defined as $x_1 = (x - 700$ mm), is used for representing the spatial PIV data in the streamwise direction.

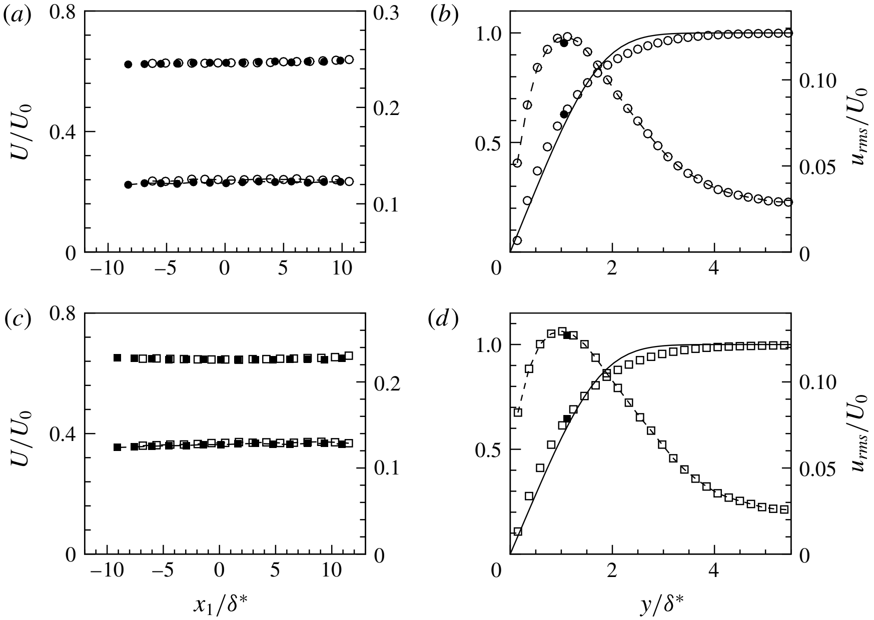

FIGURE 7. Comparison of the streamwise mean and root mean square (r.m.s.) velocities along the line of intersection of the x–y and x–z planes for grid A (a) and grid B (c). Wall-normal distribution of the mean and r.m.s. velocities at $x_1 = 0$ for grid A (b) and grid B (d); here, a single data point obtained from the spanwise plane measurements at the point of intersection is also shown in the corresponding distribution as a single filled symbol. Symbols: circle, grid A; square, grid B. Filled symbols, x–z plane data; open symbols, x–y plane data. Symbols with dashed line, u_{rms}/U_0 data; symbols without line, U/U_0 data; ——, Blasius profile.

Similarly to Hambleton *et al.* (2006), the streamwise mean and r.m.s. velocities, obtained from the simultaneous measurements in the x–y and x–z planes at the line of intersection, are compared in figure 7. Comparisons of the mean and r.m.s. velocities along the streamwise direction at $y = 2.5$ mm and $z = 0$ mm are shown in figures 7(a) and 7(c) for grids A and B respectively. Figures 7(b) and 7(d) display the wall-normal distribution of these velocities at $x = 700$ mm, along with the corresponding data (single filled point) obtained from the x–z plane measurements at $y = 2.5$ mm, for grids A and B respectively. These results reveal clear correspondence between the spanwise plane and the wall-normal plane data of our simultaneous measurements. We may also mention that the mean velocity variation in the z-direction is found to be negligible.

Some instantaneous PIV realizations, which are simultaneously acquired in both the x–y and x–z planes, are shown in figure 8. In this figure, the arrows over the contours of the normalized instantaneous velocity, U_I/U_0, indicate the fluctuating velocity vectors in the respective measurement planes. In this section, the white dashed lines in the x–z and x–y plane views show the locations of the x–y and x–z measurement planes respectively. Since the streamwise fluctuating velocity, u, is large compared with the wall-normal and spanwise fluctuating velocities, v and w respectively, these perturbations are called negative u fluctuations and positive u fluctuations based on the sign of the fluctuations (Mandal *et al.* 2010). However, Jacobs & Durbin (2001) and Zaki & Durbin (2005) identified these fluctuations as

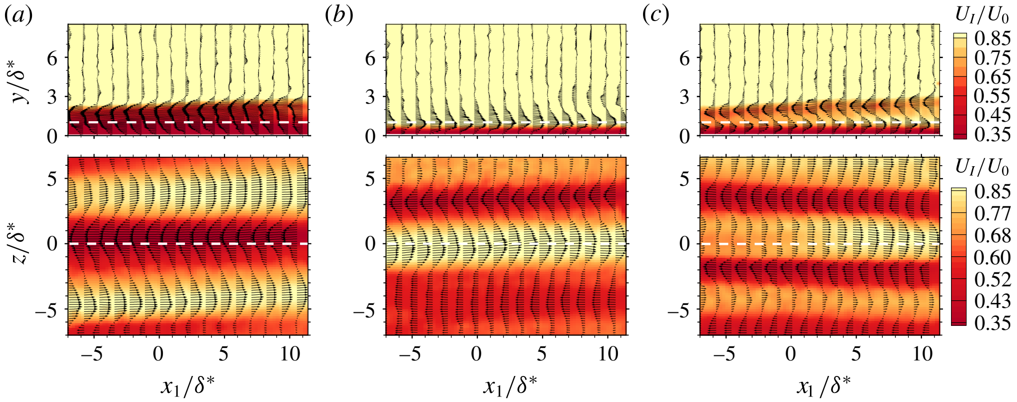

FIGURE 8. (Colour online) Quantitative and simultaneous visualizations of an instantaneous low-speed streak (*a*), an instantaneous high-speed streak (*b*) and an instantaneous low-speed streak residing over a high-speed streak (*c*) in the x–y and x–z planes for grid A. The arrows are the fluctuating velocity vectors over the contours of the normalized instantaneous streamwise velocity. The vectors, some of which are skipped for clarity, are in the same relative scale for each panel.

backward jets and forward jets. In their review article, Durbin & Wu (2007) clarified that the contours of u reveal the boundary layer streaks as long and narrow structures, while these are not apparent in the contours of the v component, and, therefore, these are rightly called jets. From their PIV measurements in bypass transition in one plane at a time, Mandal *et al.* (2010) stated that these positive and negative u fluctuations can arise due to the unsteady low- and high-velocity streaks in the boundary layer respectively. The present simultaneous measurements explicitly show that the negative u fluctuations in the wall-normal plane correspond to a low-speed streak and the positive u fluctuations in the wall-normal plane correspond to a high-speed streak in the boundary layer, as displayed in figures 8(*a*) and 8(*b*) respectively. Interestingly, we also find that a low-speed streak can completely reside over a high-speed streak, as shown in figure 8(*c*). This may be because of the fact that the low-velocity fluid from the two lifted-up low-speed streaks residing on either side of a near-wall high-speed streak can spread over it due to the spanwise meandering motions of the boundary layer streaks.

For better presentation of the transitional flow features in either a flat boundary layer flow or a channel/pipe flow, various authors (Nishioka, Asai & Iida 1981; Rist & Fasel 1995; Reuter & Rempfer 2004) have considered the contours of the wall-normal shear to investigate the late-stage transitional events. Similarly to these canonical transitional flows, the presence of inclined shear layers in bypass transition has also been reported in the literature (e.g. Mandal *et al.* 2010; Nolan & Walsh 2012; Phani Kumar *et al.* 2015). In their recent study on transition delay, Phani Kumar *et al.* (2015) showed that one can suppress transition by controlling these inclined shear layers in bypass transition. However, the origin of an inclined shear layer was not clear solely from a single-plane PIV measurement. The present simultaneous PIV realizations, as shown in figure 9, clearly reveal the genesis of these inclined shear layers. We may note that the wall-normal shear layer, here and in the following, is identified using the spanwise instantaneous vorticity, ω_z $(= \partial V_I/\partial x - \partial U_I/\partial y)$, as $\partial V_I/\partial x$ is small compared with $\partial U_I/\partial y$. Examination of the entire PIV realizations reveals that a lifted-up shear layer

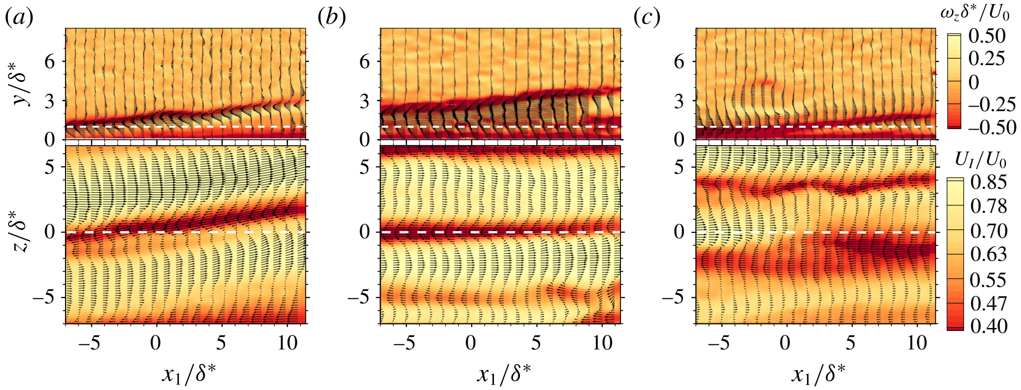

FIGURE 9. (Colour online) Three simultaneous PIV realizations depicting the origin of inclined shear layers, due to the inclination of the boundary layer streaks in the spanwise plane (*a*), due to a narrowing low-speed streak (*b*) and due to the interaction of high- and low-speed streaks (*c*), for grid A. The arrows are the fluctuating velocity vectors over the contours of the normalized vorticity and the normalized instantaneous velocity in the x–y and x–z planes respectively. The vectors, some of which are skipped for clarity, are in the same relative scale for each panel.

can originate while a pair of low- and high-speed streaks are inclined with respect to the x-direction, as shown in figure 9(*a*), or while a low-speed streak becomes narrower in the downstream direction due to the high-speed streaks on its sides, as shown in figure 9(*b*), or while a high-speed streak interacts with a low-speed streak, as shown in figure 9(*c*). It was also observed that an inclined shear layer can appear due to the occurrence of a low-speed streak over a high-speed streak, i.e. for the case in figure 8(*c*).

The streaks in bypass transition are unsteady in nature, and these streaks while moving downstream often show slow movements in the spanwise direction as well. These slow spanwise movements of the streaks, which cause the low-frequency oscillations in the streamwise velocity in bypass transition, are often referred to as streak meandering in the literature (e.g. Schlatter *et al.* 2008; Pasquale & Rona 2010). Therefore, the different streak configurations, as seen in figure 9 in the x–z plane visualizations, can be attributed to the spanwise meandering motion of the boundary layer streaks. Since the shear layer thicknesses associated with low- and high-speed streaks are different (Mandal *et al.* 2010), their inclined occurrence/interaction along the x-direction results in an inclined shear layer in the x–y measurement plane, as seen in figure 9(*a*,*c*). On the other hand, the fluctuating velocity vectors in figure 9(*b*) reveal that the magnitude of the negative u fluctuations associated with the low-speed streak at around $z = 0$ in the x–z plane reduces sluggishly in the x-direction. That is, the gain in the instantaneous velocity, U_I, is not significant in the streamwise direction, as $u = U_I - U$. Therefore, the low-speed fluid of the streak, constricted by two high-speed streaks on either side, has to gradually lift up to maintain the mass conservation of the low-speed fluid. This gradual lift-up of the low-speed fluid towards the boundary layer edge eventually leads to an inclined shear layer in the wall-normal plane.

Previous studies using flow visualizations and PIV measurements in the spanwise plane have revealed the existence of sinuous and varicose streak instabilities in bypass transition (e.g. Matsubara & Alfredsson 2001; Mans *et al.* 2005, 2007).

However, to the best of our knowledge, no experimental work on bypass transition induced by free-stream turbulence exists that shows the wall-normal flow features corresponding to sinuous and varicose streak oscillations in the spanwise plane. Since these oscillations appear randomly in the flow, one needs to utilize the simultaneous dual-plane measurements to characterize these flow features. Moreover, these random instability wavepackets can occur at any spanwise location. Therefore, a large number of simultaneous PIV realizations were acquired to ensure the occurrence of a considerable number of instability wavepackets exactly at the location of the wall-normal plane laser sheet, i.e. at $z = 0$. This cumbersome exercise of simultaneous measurements is essential to avoid misleading viewpoints, as mentioned earlier in this paper.

Figure 10 depicts wall-normal views corresponding to sinuous and varicose streak oscillations in the spanwise plane. One may clearly notice that the sinuous instability of a low-speed streak in the spanwise plane corresponds to highly oscillating shear layers in the wall-normal plane, as seen in figure 10(*a*,*b*). Shear layer roll-up and associated vortex shedding can also be observed in these figures. Similarly, figure 10(*c*,*d*) shows the wall-normal views corresponding to the varicose streak instability in the spanwise plane. We notice that the varicose instability also develops over a low-speed streak like the sinuous instability, and leads to shear layer oscillations in the wall-normal plane. In this case, the shear layer oscillations are found to occur a little closer to the wall compared with the ones in figure 10(*a*,*b*). Moreover, the shear layer oscillations corresponding to the sinuous and varicose instabilities are also found to be similar to the ones simulated by Brandt (2007) (see his figure 13) and Brandt *et al.* (2004) (see their figures 13 and 16). We may also mention that a larger number of sinuous oscillations were captured using the present measurement configuration, perhaps because of their more unstable nature compared with the varicose oscillations.

These instabilities in the low-speed streak more often lead to significant detached vorticities and counter-rotating vortex pairs in the x–y plane, as can be seen in figure 11(*a*,*b*). On the other hand, detached spanwise vorticity and counter-rotating vortex pairs in the x–y plane usually correspond to an incipient turbulent spot (see Singer 1996; Mandal *et al.* 2010, for example). Moreover, these sinuous streaks in the x–z plane are closely comparable with the nonlinearly saturated sinuous streaks of Konishi & Asai (2010), who studied the growth and breakdown of sinuous subharmonic streaks generated in a controlled manner in a zero-pressure-gradient boundary layer (see their figures 6 and 10, for example). Therefore, the sinuous streak oscillations in the x–z plane, as shown in figure 11(*a*,*b*), are associated with an incipient turbulent spot.

Some numerical works on bypass transition (e.g. Jacobs & Durbin 2001; Schlatter *et al.* 2008; Hack & Zaki 2014) indicate that the secondary instability in the boundary layer streaks can get excited near the boundary layer edge. Experimental verification of such scenarios can be made possible with the aid of simultaneous dual-plane PIV measurement. Figure 12(*a*,*b*) clearly shows shear layer oscillations towards the outer side of the boundary layer in the x–y plane. However, no appreciable varicose or sinuous oscillation of the corresponding streak in the x–z plane can be noticed. Several such scenarios are found to exist in the entire PIV realizations. Compared with figure 12(*a*,*b*), the shear oscillations, as shown in figure 12(*c*,*d*), are closer to the x–z measurement plane at $y = 2.5$ mm, and the signature of varicose and sinuous oscillations in the underlying low-speed streaks can clearly be noticed in the corresponding x–z plane views. Therefore, one would have

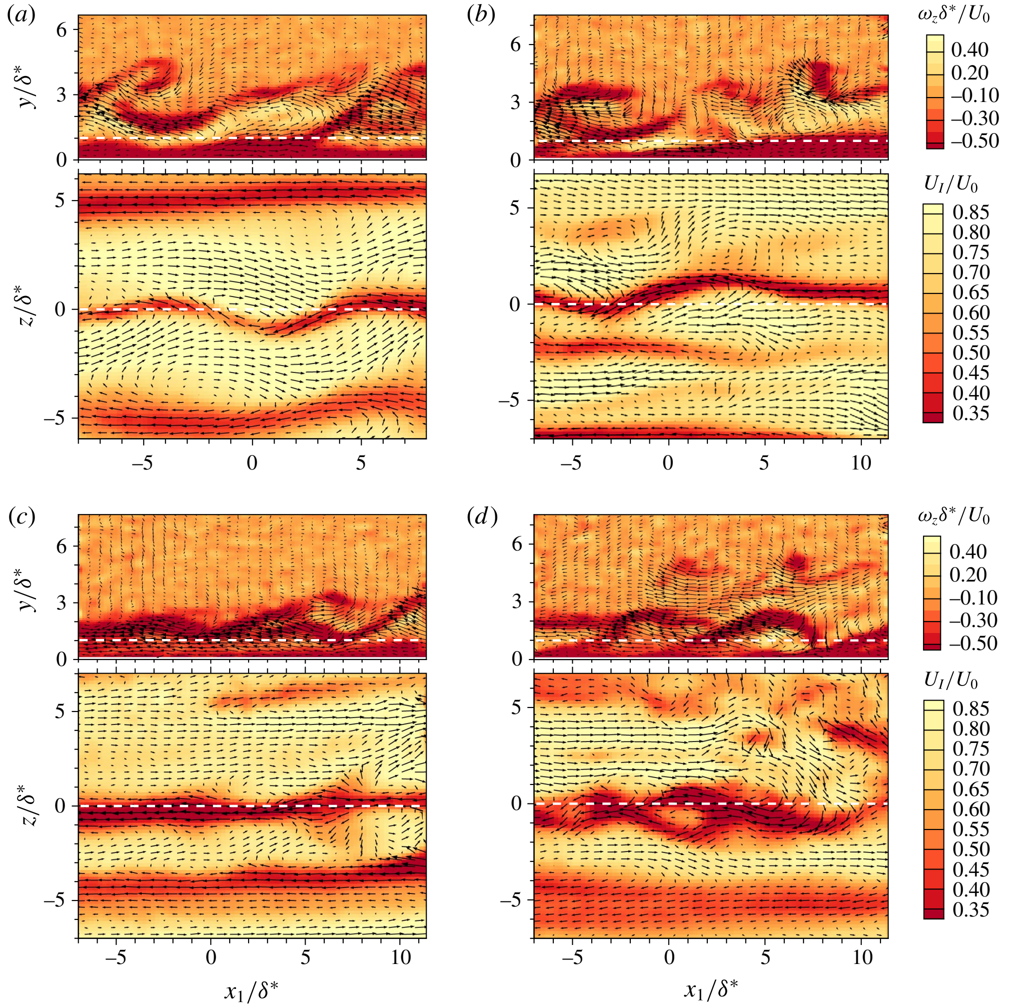

FIGURE 10. (Colour online) The x–y plane views corresponding to sinuous (a,b) and varicose (c,d) instabilities in the x–z plane for grid A. The arrows are the fluctuating velocity vectors over the contours of the normalized vorticity and the normalized instantaneous velocity in the x–y and x–z planes respectively. The vectors, some of which are skipped for clarity, are in same relative scale for each panel.

noticed varicose/sinuous instability in the x–z plane corresponding to the shear layer oscillations in figure 12(a,b) if the x–z measurement plane were shifted towards the boundary layer edge for those cases. Otherwise, the amplitude of a shear layer oscillation should be high enough so that the spanwise streaks in the x–z plane at $y = 2.5$ mm are influenced, although there exists a possibility that the shear layer will get distorted due to its large oscillation, as seen in figure 10(a,b) for example. Hence, the present simultaneous measurements, as shown in figure 12, clearly indicate that the secondary instability on a low-speed streak can get excited near the edge of the boundary layer.

In general, the shear layer oscillations in the x–y plane corresponding to the varicose streak oscillations in the x–z plane are often found to be closer to the wall compared

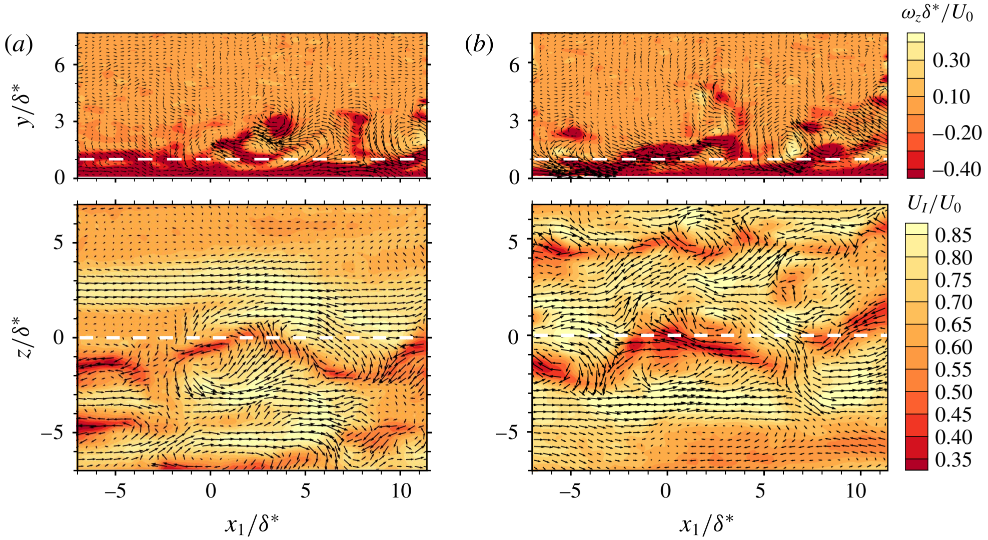

FIGURE 11. (Colour online) (*a*,*b*) The *x*–*y* plane views corresponding to two saturated sinuous streaks in the *x*–*z* plane for grid A. The arrows are the fluctuating velocity vectors over the contours of the normalized vorticity and the normalized instantaneous velocity in the *x*–*y* and *x*–*z* planes respectively. The vectors, some of which are skipped for clarity, are in the same relative scale for each panel.

with the shear layer oscillations corresponding to the sinuous streak oscillations in the *x*–*z* plane; for example, see figures 10 and 12. These observations are also found to be similar to the recent numerical findings of Vaughan & Zaki (2011) and Hack & Zaki (2014), who reported that an outer mode, which is predominantly of sinuous nature, occurs towards the outer edge of the boundary layer, whereas an inner mode, which is mainly of varicose nature, occurs closer to the wall.

5. Time-resolved PIV data

In this section, results of the TR-PIV measurements, performed independently in the *x*–*y* and *x*–*z* planes, are discussed in detail. Centring the camera at $x = 700$ mm, the TR-PIV data were acquired at 645 Hz, as stated in § 2.2. Usually, the streaky structures in bypass transition are low-frequency structures with non-dimensional frequency $F(= 2\pi f\nu \times 10^6/U_0^2) \leqslant 35$ (Westin *et al.* 1994). The corresponding dimensional frequency for the present study does not exceed 15 Hz, and the frequencies of approximately 95 % of the secondary instability events considered in this work are found to be well within 300 Hz. Further, simultaneous hotwire and TR-PIV measurements were also carried out to investigate the correspondence between the hotwire and TR-PIV velocity signals. The velocity time series extracted from the TR-PIV data was found to be comparable with the one obtained from the hotwire, as illustrated in figure 13. The slight phase shift and the small difference in magnitude between these two signals are due to the fact that the TR-PIV data were collected approximately 2 mm ahead of the hotwire probe, because particle images at the probe location cannot be processed due to reflection from the probe, as illustrated in the inset of figure 13. Although an acquisition rate higher than 645 Hz could have been achieved by compromising further the spatial resolution of the camera,

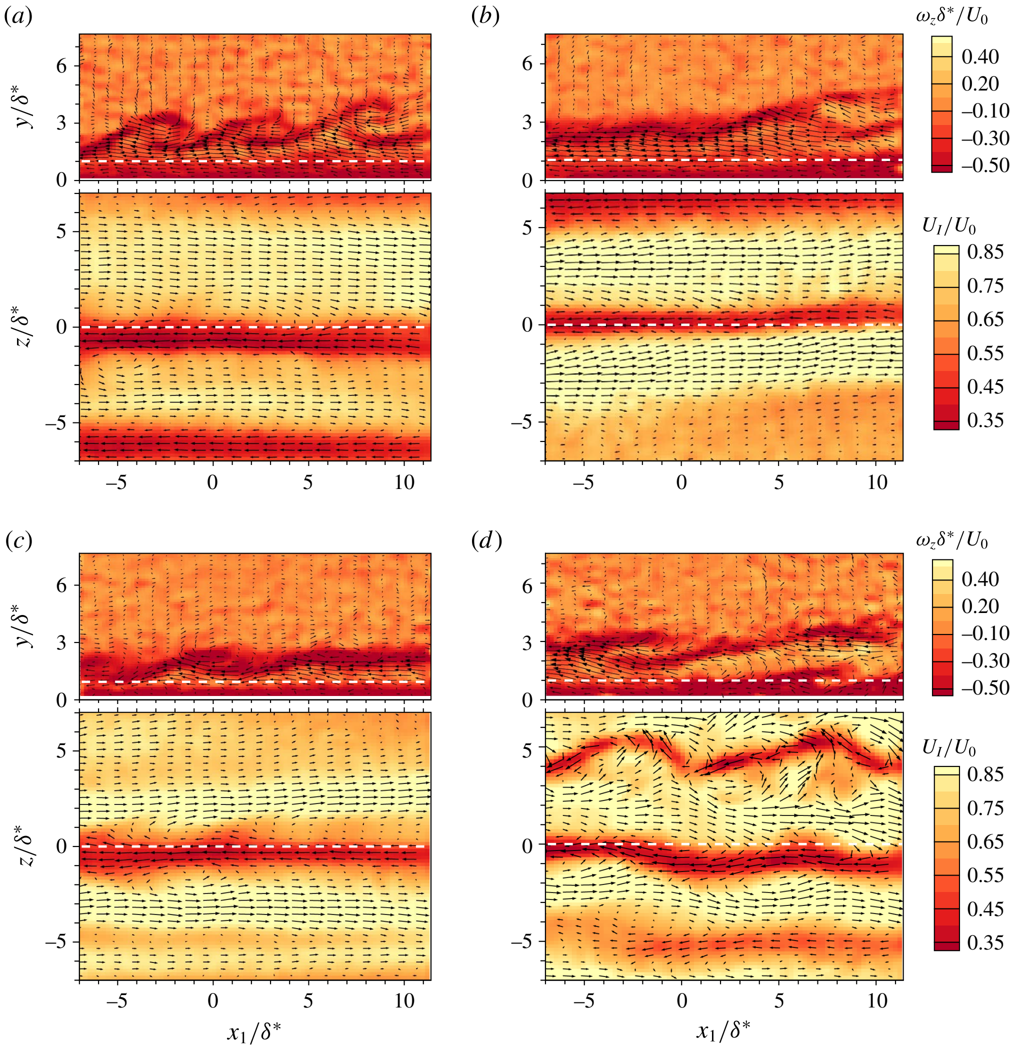

FIGURE 12. (Colour online) (*a*,*b*) Two instantaneous PIV realizations illustrating oscillating shear layers in the *x*–*y* plane while no significant oscillations in the underlying boundary layer streaks in the *x*–*z* plane. (*c*,*d*) Two instantaneous PIV realizations illustrating oscillating shear layers in the *x*–*y* plane corresponding to varicose and sinuous oscillations in the underlying boundary layer streaks in the *x*–*z* plane respectively. The arrows are the fluctuating velocity vectors over the contours of the normalized vorticity and the normalized instantaneous velocity in the *x*–*y* and *x*–*z* planes respectively. The vectors, some of which are skipped for clarity, are in the same relative scale for each panel. The data presented in (*a*) and (*b*) correspond to grids A and B respectively; the data presented in (*c*) and (*d*) correspond to grid A.

the present acquisition rate was found to be sufficient for investigation of the flow features under consideration. The measurements were carried out at nearly the same free-stream velocities as presented in table 4 for grids A and B. With the available inboard memory of the CMOS camera, 1250 TR-PIV realizations were acquired in one run of the measurement. Since the instability events in bypass transition are

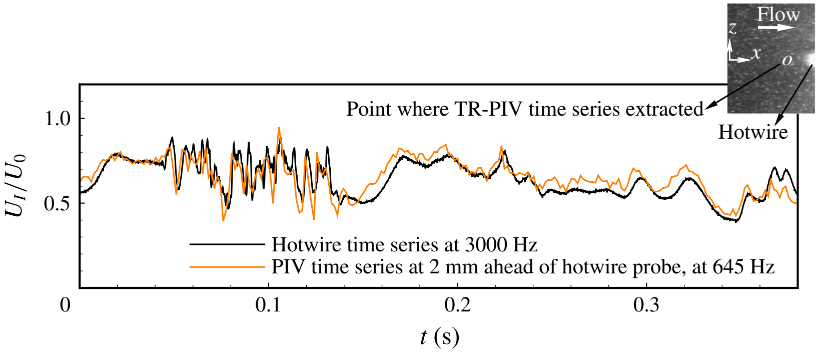

FIGURE 13. (Colour online) Comparison of hotwire and TR-PIV time series of intermittent signals at the end of the TR-PIV measurement zone. Both signals are simultaneously acquired at the plate centreline and at $y = 2.5$ mm. The inset illustrates the particle images and hotwire location.

random in nature, a total of 13 such runs in the x–y plane and 15 such runs in the x–z plane were conducted for detailed statistical data analyses of these instability events for grids A and B.

5.1. *Instability of the lifted-up shear layers in the x–y plane*

The simultaneous dual-plane PIV measurements presented in figure 12 indicate that the sign of an instability first gets manifested as shear layer oscillation in the x–y plane. Therefore, it is interesting to track these shear layer oscillations at different instants of time to investigate their eventual outcome.

A time sequence of flow features associated with a lifted-up shear layer and its eventual outcome is displayed in figure 14. The arrows in this figure are the fluctuating velocity vectors over the contours of the normalized spanwise instantaneous vorticity. In this figure, one may clearly see the onset of an oscillation in an almost straight shear layer followed by its amplification in space and time. One may also notice that this oscillation is developing near the leading edge of the inclined shear layer, which eventually ends up with rolled-up vortices with clockwise rotation. Several numerical studies on bypass transition (e.g. Brandt *et al.* 2004; Schlatter *et al.* 2008; Hack & Zaki 2014) have revealed the existence of three-dimensional vortical structures over the oscillating low-speed streaks. The present rolled-up vortices may represent the wall-normal view of these three-dimensional vortical structures. However, one may also observe in the last few snapshots of figure 14 that while the clockwise vortices come close to the wall and interact with a high-speed streak, some pairs of clockwise and anticlockwise vortices are formed. These counter-rotating vortex pairs, while propagating over positive u fluctuations, i.e. over a high-speed streak, are found to grow in size and destabilize the underlying high-speed streak and generate smaller scales in the flow, as illustrated in figure 15. The sequence of events from the time-resolved measurements, as shown in figures 14 and 15, therefore, clearly confirms the previous speculation that an incipient spot can be formed from an inclined shear layer oscillation and its associated vortex shedding (Mandal *et al.* 2010).

In contrast to the oscillation in figure 14, which develops at the leading edge of an inclined shear layer, figure 16 displays an oscillation that develops near the

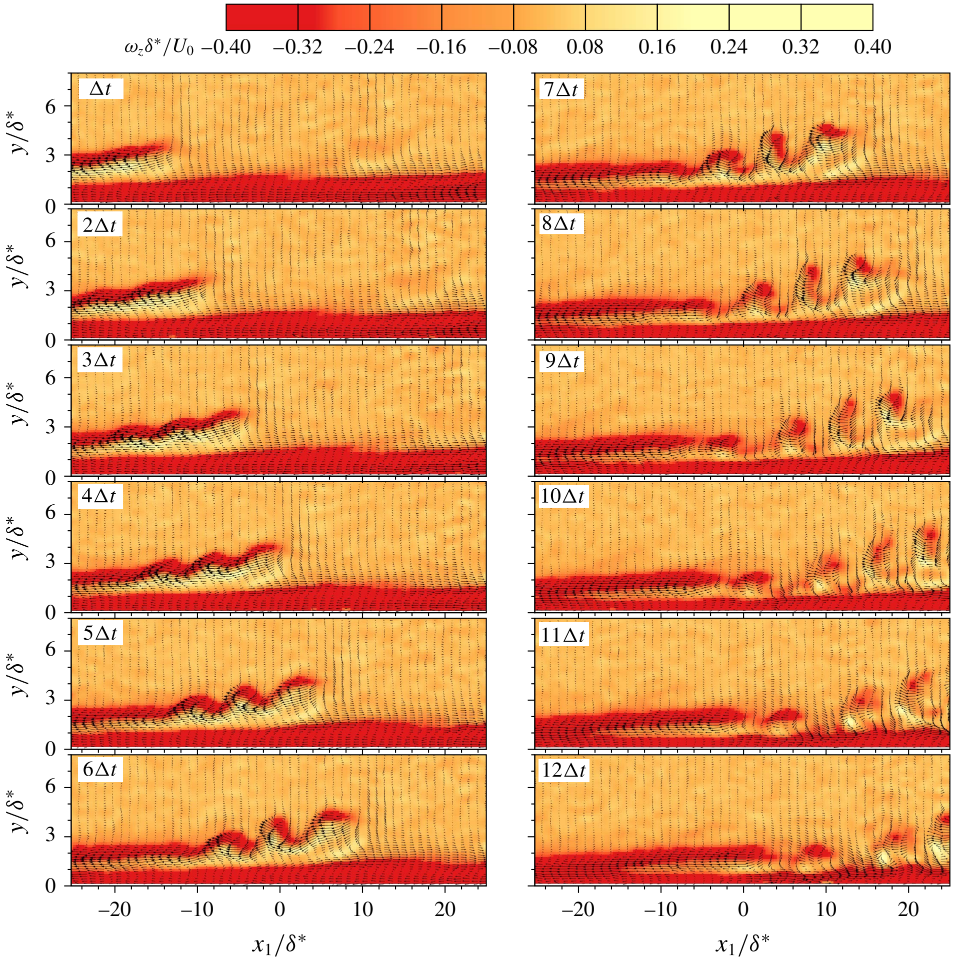

FIGURE 14. (Colour online) Sequence of TR-PIV snapshots displaying the development of an instability over a lifted-up low-speed streak in the x–y plane for grid B. The contours correspond to the normalized spanwise vorticity. The vectors represent the fluctuating velocity vectors. Each snapshot is separated by $\Delta t = 0.00155$ s.

trailing edge, i.e. almost at the start of its inclination with the wall. Moreover, these oscillations are found to occur a little closer to the wall compared with those in figure 14, and their amplification eventually generates some smaller inclined shear layers, as seen at the $12\Delta t$ instant in figure 16. However, these oscillations are also found to take part in generating smaller scales in the flow.

It would have been interesting if simultaneous spanwise plane views corresponding to the flow features presented in figures 14 and 16 were available to investigate how these time sequences are related to the streak oscillations in the spanwise plane. However, in the absence of such measurements, we refer to our simultaneous measurements for further comprehensive assessment of the data presented in figures 14 and 16. The shear layer oscillations in figure 14 (for example, realizations at $7\Delta t$ and $8\Delta t$ instants) are found to be similar to those shown in figure 10(a,b), which are related to the sinuous streak instability in the x–z plane. Therefore, if one could have

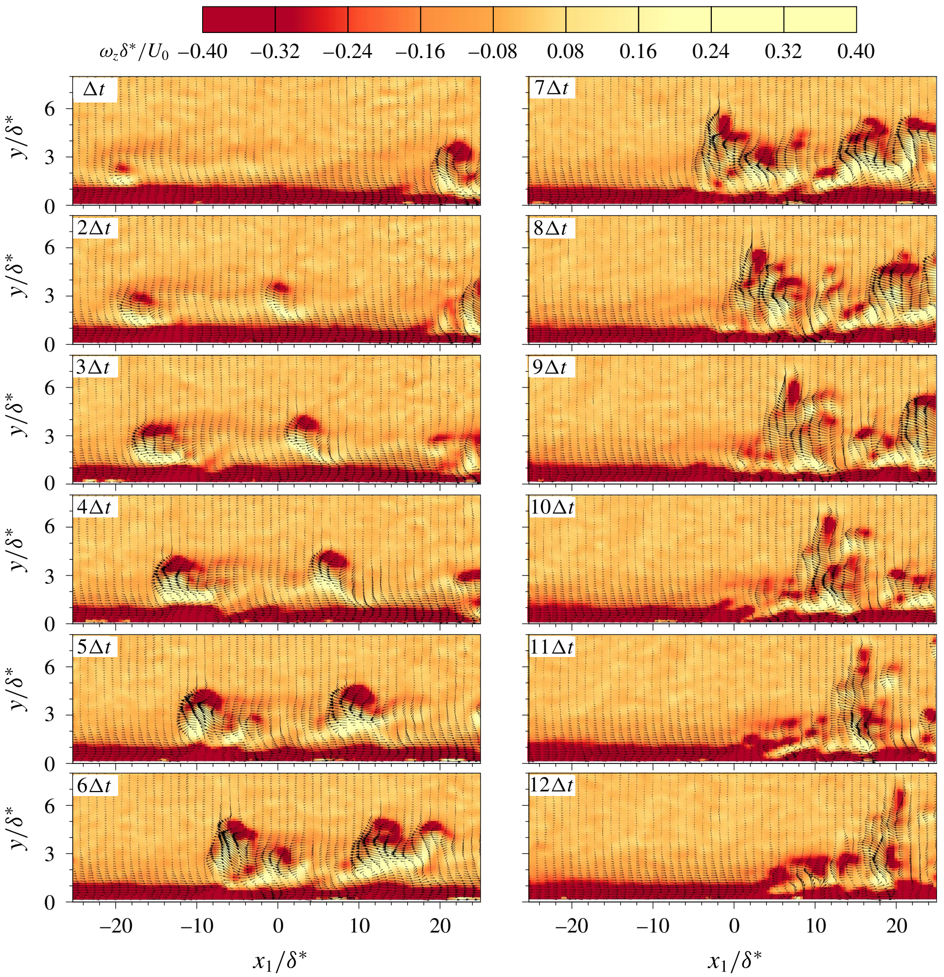

FIGURE 15. (Colour online) Sequence of TR-PIV snapshots displaying flow randomization through the propagation of clockwise–anticlockwise vortex pairs over a high-speed streak in the x–y plane for grid B. The contours correspond to the normalized spanwise vorticity. The vectors represent the fluctuating velocity vectors. Each snapshot is separated by $\Delta t =$ 0.00155 s.

measured the spanwise data corresponding to the time sequence shown in figure 14, one would have seen sinuous instability in the x–z plane. Further, the shear layer oscillations in figure 16 (for example, realizations at the $11\Delta t$ and $12\Delta t$ instants) are similar to those in figures 10(c,d) and 12(c). Therefore, these oscillations are most likely related to the varicose streak instability in the x–z plane.

5.1.1. *Linear stability analysis*

The time sequences in figures 14 and 16 indicate that an instability develops on a low-speed streak, as the fluctuating velocity vectors associated with the inclined shear layers show large negative u fluctuations. The instantaneous velocity profiles, as seen from the instantaneous velocity vectors associated with these shear layers, are found to be highly inflectional, as shown in figure 17(a,c) at the Δt time instant. This implies

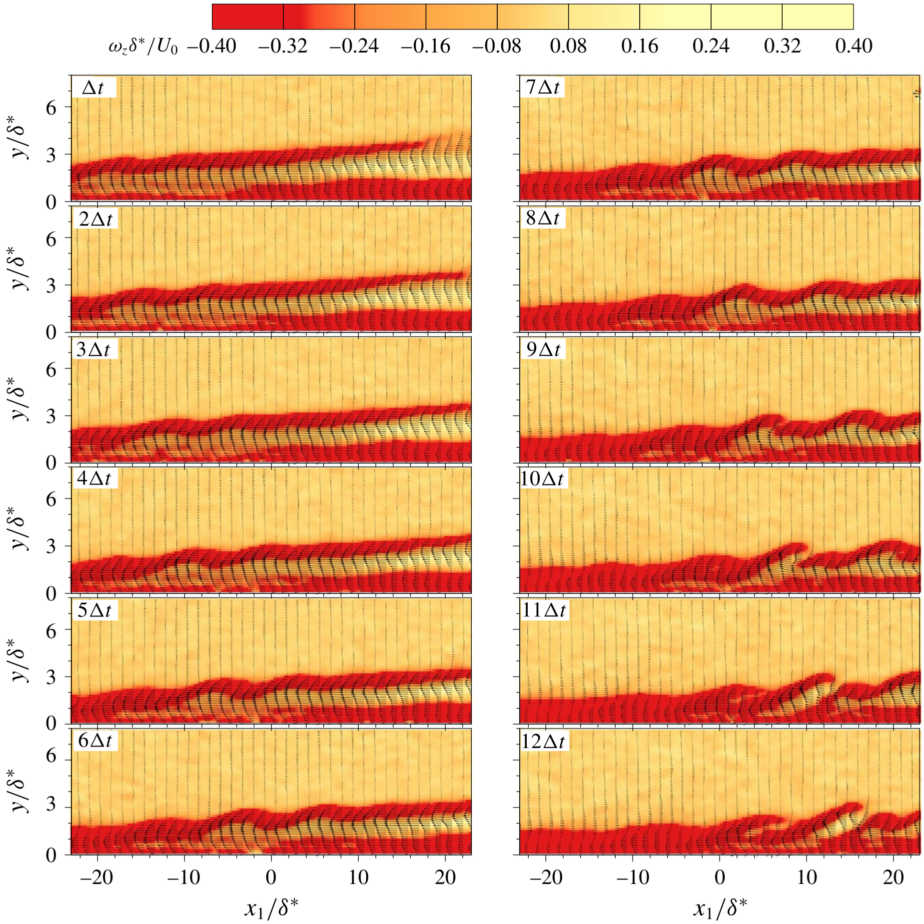

FIGURE 16. (Colour online) Sequence of TR-PIV snapshots displaying the development of an instability nearly at the trailing edge of an inclined shear layer in the x–y plane for grid B. The contours correspond to the normalized spanwise vorticity. The vectors represent the fluctuating velocity vectors. Each snapshot is separated by $\Delta t = 0.00155$ s.

that these shear layers may be prone to inflectional instability, and a local linear instability analysis may be useful in predicting the frequency and wavelength of their oscillations. In such an effort, Hack & Zaki (2014) utilized the instantaneous velocity data in the y–z plane for two-dimensional linear stability analysis (2D-LSA), i.e. $U_I(y, z)$ as the base profile that includes the effect of spanwise shear. They found that the theoretical growth rate closely follows the estimated spatio-temporal growth rate from their DNS data. However, their linear stability and statistical analyses indicate that the growth rate of a base streak is well correlated with the wall-normal shear and the base streak amplitude, whereas it is poorly correlated with the spanwise shear. This indicates that the stability analysis of the wall-normal velocity profile itself, i.e. $U(y)$ as the base profile that does not include the effect of spanwise shear, may be useful in providing elementary stability characteristics of these shear layer oscillations.

For example, in their experimental study on boundary layer transition, Asai *et al.* (2002) carried out one-dimensional linear stability analysis (1D-LSA) of the mean

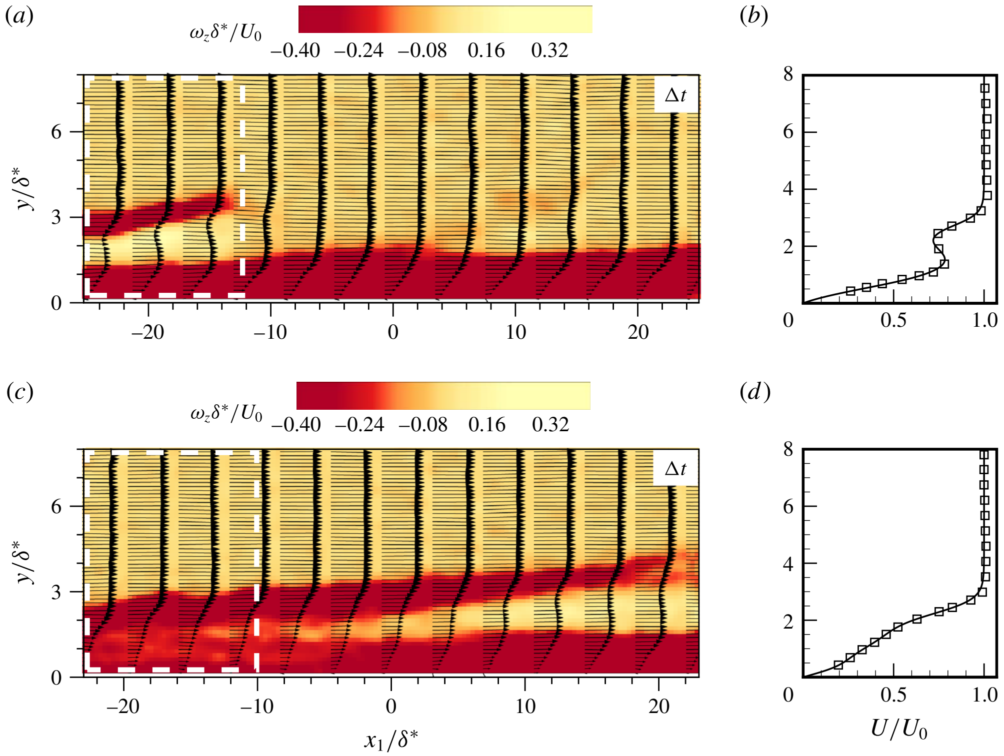

FIGURE 17. (Colour online) (*a*,*c*) Illustrations of the inflectional nature of the instantaneous velocity vectors corresponding to the shear layers in figures 14 and 16 at the Δt instant of time respectively. The contours represent the normalized spanwise vorticity. (*b*,*d*) Spatially averaged velocity data (symbols) over the white rectangular regions in (*a*,*c*) respectively, along with the fitted velocity profiles (solid line) using (5.1); grid B data.

velocity profile of a low-speed streak by fitting a tangent-hyperbolic curve. They found that the calculated most amplified frequency and the corresponding wavenumber compared well with their measured counterparts. In this regard, the numerical reproduction of the experimental work of Asai *et al.* (2002) reported by Brandt (2007) is worth mentioning. Using the perturbation kinetic energy analysis, he found that both sinuous and varicose instabilities are governed by the work of the Reynolds stress against the wall-normal shear, and this is contrary to the common belief that sinuous and varicose instabilities are driven by the streak spanwise and wall-normal shears respectively. Similarly, Philip, Karp & Cohen (2016) carried out linear stability analysis of a streaky base flow measured in a laminar plane Poiseuille flow. Neglecting the spanwise shear, they carried out 1D-LSA and found that their stability results (i.e. wavelength, eigenfunction shape) compared well with their experimental data. Further, their 2D-LSA and energy balance analysis indicated that the wall-normal shear is more important than the spanwise shear for producing symmetric varicose mode. Moreover, the 1D-LSA in bypass transition may be justified based on the fact that not all of the streaks in the spanwise direction simultaneously develop instability; rather, the instability in a natural bypass transition is localized in nature (e.g. Hack & Zaki 2014), i.e. it is often seen to develop on a single low-speed streak, in contrast to the collective instability on the entire row of streaks as considered by Andersson *et al.* (2001) and Vaughan & Zaki (2011).

The boundary layer streaks in bypass transition are highly unsteady in nature compared with the controlled ones considered by Asai *et al.* (2002) and Philip *et al.* (2016). Hence, the usual ensemble average or time average data cannot provide a mean velocity profile corresponding to a particular low-speed streak that eventually develops instability. Therefore, a base velocity profile is obtained here by spatial averaging of the instantaneous velocity profiles over a distance of $10\delta^*$–$15\delta^*$ for a single low-speed streak on which instabilities like those in figures 14 and 16 develop. Then, the spatially averaged velocity profile is fitted with a tangent-hyperbolic profile, following Asai *et al.* (2002), for the local linear stability analysis. The tangent-hyperbolic profile

$$\frac{U\,(y)}{U_L} = a_1 \tanh\left(b_1 \frac{y}{\delta_L^*} - c_1\right) + a_2 \tanh\left(b_2 \frac{y}{\delta_L^*} - c_2\right) + a_3 \tanh\left(b_3 \frac{y}{\delta_L^*} - c_3\right) + d \quad (5.1)$$

was found to describe the spatially averaged mean velocity data quite well; here, a_1, a_2, a_3, b_1, b_2, b_3, c_1, c_2, c_3 and d are constants; the local free-stream velocity, U_L, and the displacement thickness, δ_L^*, are estimated based on the spatially averaged velocity profile.

The above procedure is illustrated in figure 17. All of the instantaneous velocity profiles within the white rectangular regions in figure 17(*a*,*c*) are spatially averaged, and (5.1) has been used to fit the respective averaged velocity profiles. The fitted curves are found to closely follow the measured data, as shown in figure 17(*b*,*d*). Although there are several constants in (5.1), these constants can easily be determined by a trial and error approach in MATLAB. The numerical values of $\{a_1, a_2, a_3, b_1, b_2, b_3, c_1, c_2, c_3, d\}$ for the velocity profiles in figure 17(*b*,*d*) are found to be {0.518, 1.698, 0.8207, 0.1085, −2.4, −4.08, 0.175, 2.45, 6.02, 0.4155} and {0.1995, 3.9, 0.1721, 0.1155, 2.88, 2.05, 0.2695, 2.8, 4.25, 0.4155} respectively.

For stability analysis on the fitted velocity profiles, the Orr–Sommerfeld equation, following Boutilier & Yarusevych (2012), is written as

$$(\alpha U - \omega)\left[\phi'' - \alpha^2\phi\right] - \alpha U''\phi = -\frac{\mathrm{i}U_L\delta_L^*}{Re_{\delta_L^*}}\left[\phi'''' - 2\alpha^2\phi'' + \alpha^4\phi\right]. \quad (5.2)$$

Here, ϕ and ϕ' denote the complex amplitude function of the wall-normal perturbation velocity, i.e. $v = \phi(y)\mathrm{e}^{\mathrm{i}(\alpha x - \omega t)}$, and its derivative with respect to y respectively. The wavenumber, angular frequency and Reynolds number are denoted by α, ω and $Re_{\delta_L^*}(= U_L\delta_L^*/\nu)$ respectively. The above equation (5.2) is solved with the boundary conditions $\phi(0) = \phi(\infty) = 0$ and $\phi'(0) = \phi'(\infty) = 0$. Similarly, for inviscid stability analysis, the Rayleigh equation

$$(\alpha U - \omega)\left[\phi'' - \alpha^2\phi\right] - \alpha U''\phi = 0 \quad (5.3)$$

is solved with the boundary conditions $\phi(0) = \phi(\infty) = 0$. Both the Orr–Sommerfeld and the Rayleigh equation are posed as spatial eigenvalue problems considering the wavenumber, $\alpha = \alpha_r + i\alpha_i$, as complex and the angular frequency, ω, as real, and these equations are then solved using the spectral method (Schmid & Henningson 2001). The details of this method and the solution procedure are given in Dabaria (2015).

The growth rate, wavenumber and phase velocity obtained by solving the Orr–Sommerfeld and Rayleigh equations at various circular frequencies are displayed in figures 18(*a*–*c*) and 18(*e*–*g*) for the velocity profiles in figures 17(*b*) and 17(*d*) respectively. The eigenfunctions corresponding to the streamwise velocity perturbation

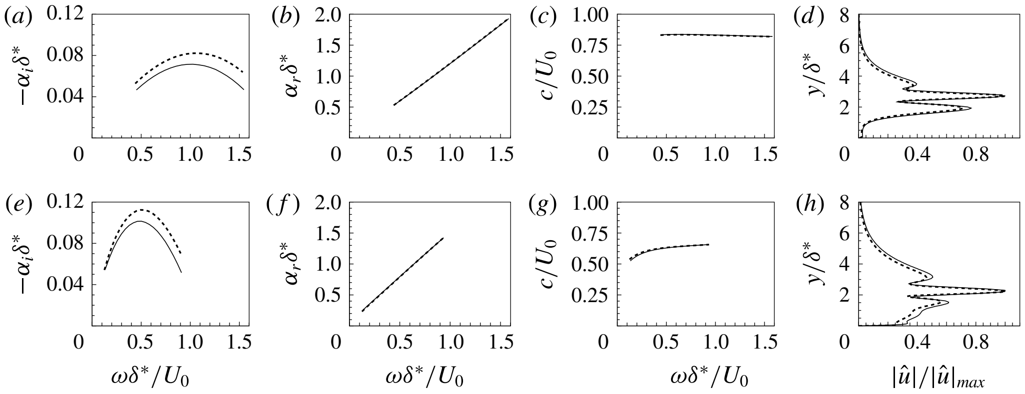

FIGURE 18. (*a–d*) Spatial growth rate, wavenumber, phase velocity and magnitude of u eigenfunction $|\hat{u}|$ respectively for the velocity profile in figure 17(*b*). (*e–h*) Spatial growth rate, wavenumber, phase velocity and magnitude of u eigenfunction $|\hat{u}|$ respectively for the velocity profile in figure 17(*d*). Solid line, Orr–Sommerfeld calculation; dashed line, Rayleigh calculation.

are also shown in figure 18(*d*) and 18(*h*), for the velocity profiles in figure 17(*b*) and 17(*d*), respectively. One may notice that the stability results for a particular velocity profile calculated based on the Orr–Sommerfeld and Rayleigh equations are comparable except for the growth rates, which are found to be higher for the inviscid stability calculations (see figure 18*a*,*e*). However, the most amplified frequencies calculated based on the Orr–Sommerfeld and Rayleigh equations are found to be nearly equal for each of the velocity profiles considered.

Since the oscillations in the shear layers are prominent, as seen in figures 14 and 16, one can easily estimate an average wavelength, λ, from the experimental data. Similarly, utilizing the time sequences at different instants of time, an average convection/propagation velocity, U_c, of an instability can also be estimated, and the frequency, f, can be estimated from the ratio of the convection velocity and the wavelength, i.e. U_c/λ. Using the contour levels of the normalized instantaneous vorticity for identification of a shear layer oscillation, we estimated the average wavelength and convection velocity of an oscillating shear layer from the experimental data. At different instants of time, we followed the portion of the oscillating shear layer that was initially confined within the rectangular box in figure 17(*a*,*c*). Then, considering the wavelength as the peak to peak/trough to trough distance of the oscillating shear layer at different instants of time, an average wavelength and its standard deviation were obtained. Similarly, by tracking a peak/trough of the oscillating shear layer at different instants of time and plotting its relative position with time, the convection velocity could be determined (see Mans *et al.* 2005, for details). Considering such an estimate for different peaks/troughs, an average convection velocity and its standard deviation were then obtained.

Based on the Orr–Sommerfeld equation, the calculated normalized wavelengths (λ/δ^*), corresponding to the most amplified frequency, were found to be 5.2 and 8.1 for the cases in figures 17(*b*) and 17(*d*) respectively. Following the method discussed above, the estimated wavelengths from the experimental data, for the corresponding cases, were found to be 5 and 8.4 respectively. Similarly, the calculated phase speeds (c/U_0) at the most amplified frequencies corresponding to the cases in figures

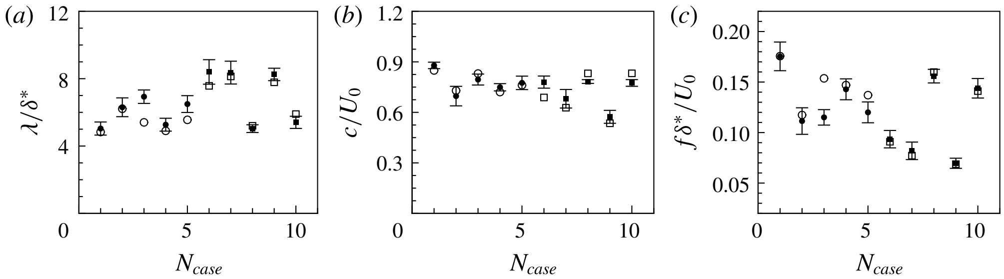

FIGURE 19. Corresponding to the maximum growth rate, comparison of the calculated wavelength (*a*), phase velocity (*b*) and frequency (*c*) with the estimated values of wavelength, convection velocity and frequency for different cases; N_{case} refers to the case index. Symbols: circle, grid A; square, grid B; open symbols, calculated data; filled symbols with error bars, estimated data.

17(*b*) and 17(*d*) were found to be 0.83 and 0.63 respectively, and the estimated convection velocities, U_c/U_0, corresponding to these cases were found to be 0.78 and 0.68 respectively. The calculated wavelengths and phase velocities compare well with the estimated values of the wavelengths and convection velocities, for both of the velocity profiles in figure 17(*b*,*d*). The maximum differences between the calculated and estimated values of the wavelength and the phase velocity are found to be 4 % and 8 % respectively. The most amplified frequencies calculated based on the Orr–Sommerfeld equation are found to be 0.16 and 0.078 for the cases in figure 17(*b*,*d*), and the estimated frequencies based on the wavelengths and the convection velocities, for the corresponding cases, are found to be 0.16 and 0.08 respectively.

Several cases like those in figures 14 and 16 were identified and linear stability analyses were carried out to investigate whether the above observations are consistent with all such cases. We identified a total of 10 such cases, as we chose only those shear layers that showed development of an instability from its inception within the field of view, and neglected those shear layers that had already developed significant oscillations before reaching the measurement field of view. Comparison of the calculated wavelengths, phase velocities and frequencies with the estimated ones is shown in figure 19, and we find similar results for all of the cases. We may note that the abscissa in figure 19 indicates the case index, N_{case}, and figure 19(*a*–*c*) also includes the data corresponding to the velocity profiles in figure 17(*b*,*d*) ($N_{case} = 8$ and 7 respectively). Hence, the results in figure 19 indicate that an oscillating shear layer is most likely to be composed of a monochromatic wave that is excited by the linear instability of the velocity profile associated with the inclined shear layer.

The numerical value of the calculated spatial growth rate ($-\alpha_i\delta^*$) for the most unstable frequency is higher for the velocity profile in figure 17(*d*) compared with the velocity profile in figure 17(*b*). On the other hand, the instability in figure 14, corresponding to the velocity profile in figure 17(*b*), seems to grow temporally faster than the instability in figure 16, corresponding to the velocity profile in figure 17(*d*). However, this is not inconsistent, as the phase/group velocity of the instability in figure 14 is higher than the phase/group velocity of the instability in figure 16 (see figure 18*c*,*g*). The shapes of the eigenfunctions for both of the velocity profiles are also found to bear some similarity to the *u* fluctuations at the later stage of the shear layer oscillations (see the fluctuating velocity vectors in figures 14 and 16 at some later stage in time).

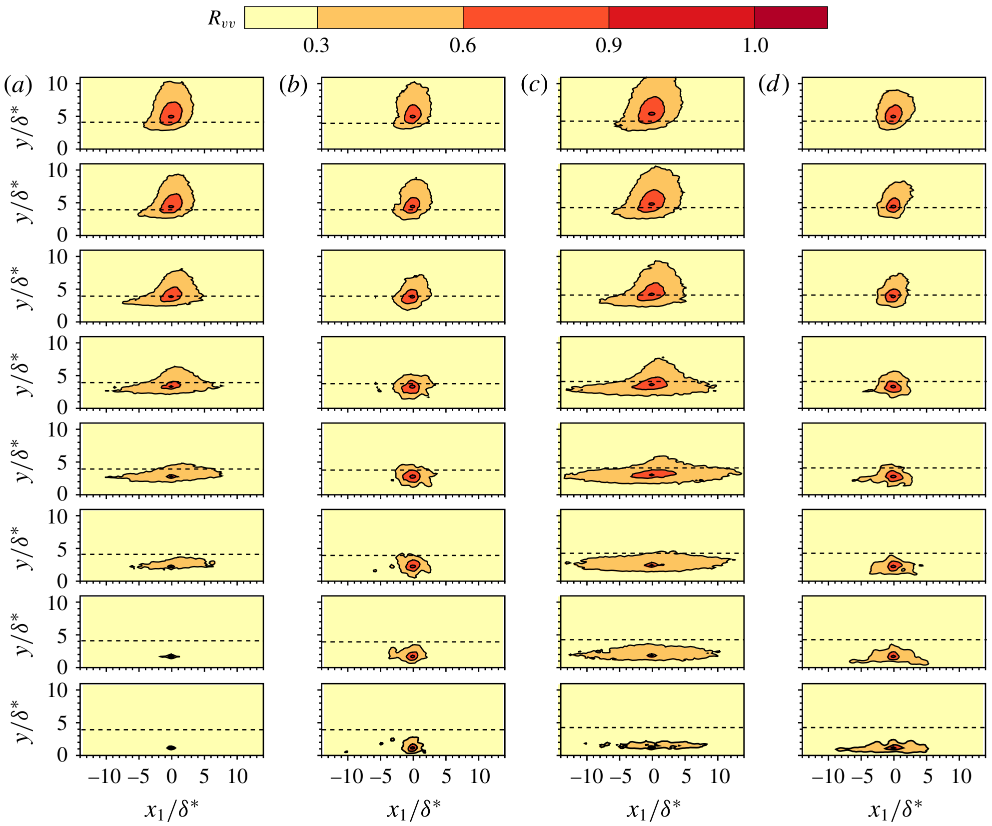

FIGURE 20. (Colour online) Contours of the spatial correlation coefficient (R_{vv}) of the wall-normal velocity fluctuations at $z = 0$; non-intermittent flow (*a*) and intermittent flow (*b*) for grid A; non-intermittent flow (*c*) and intermittent flow (*d*) for grid B. Contour levels <0.3 are omitted. The dashed line indicates the boundary layer edge.

5.1.2. *Penetration of the free-stream turbulence into the boundary layer*

The data presented in the previous sections clearly indicate the existence of an instability near the edge of the boundary layer. It would have been revealing if it were possible to establish a direct role of the free-stream turbulence in intensification of the instability process in the upper part of the boundary layer. However, it appears to be a challenging task at present as far as the measurement techniques and analysis tools are concerned. Nonetheless, using statistical analysis, it is interesting to check whether there exists any relation of the free-stream velocity fluctuations to the velocity fluctuations in the boundary layer edge. Nolan & Walsh (2012) reported that the correlation analysis of the wall-normal perturbation velocity across the boundary layer edge is a more direct representation of the penetration depth of the free-stream disturbance inside the boundary layer. Therefore, following Nolan & Walsh (2012), a spatial correlation analysis of the wall-normal perturbation velocity was carried out to investigate the possibility of an interaction.

Figure 20 shows the contours of the spatial correlation coefficient of the wall-normal disturbance velocity, defined here as $R_{vv}(\Delta x, \Delta y) = \overline{v(x_0, y_0, t)v(x_0 + \Delta x, y_0 + \Delta y, t)}/v_{rms}^2$; here x_0 and y_0 indicate the coordinates of the reference location. In this figure, the data are presented for both of the grids at two different free-stream velocities, which were chosen such that we could measure a non-intermittent flow/pre-transitional flow and an intermittent flow at the same location. The non-intermittent flows for both of the grids were measured at $U_0 = 4.1\ \mathrm{m\ s^{-1}}$ and the intermittent flows for grids A and B were measured at the velocities given in table 4. Figures 20(*a*) and 20(*c*) show the contours of R_{vv} corresponding to the measured non-intermittent flows for grids A and B respectively, whereas figures 20(*b*) and 20(*d*) display those corresponding to the intermittent flows for grids A and B respectively. For non-intermittent flows, it can be seen that the lower portion of the nearly circular correlation contours begins to elongate as the location of the reference point moves inside the boundary layer from the free stream, whereas the nearly circular shapes of the correlation contours are retained until the location of the reference point is moved very closed to the wall for intermittent flows. However, the extensions of the correlation contours across the boundary layer edge (as shown by a dashed line in figure 20) are almost the same for the intermittent and non-intermittent flows. The change of shape of the correlation contours near the boundary layer edge is due to the fact that the shear at the boundary layer edge is comparatively greater for a non-intermittent flow than the shear for an intermittent flow, as the mixing of high-momentum fluid is enhanced due to intermittent bursts of turbulent spots in an intermittent flow, and thereby reduces the velocity gradient near the boundary layer edge.

Measurements were also carried out at different spanwise locations and at different velocities to investigate the consistency of the above observation. Contours of R_{vv} at different spanwise locations and at different velocities in non-transitional flows for both of the grids are displayed in figure 21. Figure 21(*a*,*b*) shows R_{vv} contours at $U_0 = 4.1\ \mathrm{m\ s^{-1}}$ and at $z = 14$ mm and $z = -14$ mm for grids A and B respectively; it should be noted that the free-stream velocity was kept equal to the one at which the data presented in figure 20(*a*,*c*) were measured. Figure 21(*c*,*d*) shows R_{vv} contours at $U_0 = 3\ \mathrm{m\ s^{-1}}$ and at $z = 0$ mm and $z = -14$ mm for grids A and B respectively. Comparing the contours in non-intermittent flows in figures 20 and 21, one may notice a similarity in the correlation contours at different spanwise locations and at different velocities. We may also note that the R_{vv} contours in intermittent flows (not presented here) at different spanwise locations are found to be similar to those presented in figure 20(*b*,*d*).

However, the present correlation maps for intermittent flows compare well with the data of Nolan & Walsh (2012). The results for non-intermittent flows are different from those reported by them. They did not find any significant correlation of v fluctuations between the free stream and the boundary layer for non-intermittent flows. The reason for the difference from the findings of Nolan & Walsh (2012) may be because of different transition mechanisms involved in these two works. They reported the interaction between a low-speed streak and a high-speed streak to be a dominant spot precursor mechanism. In their numerical simulation of a bypass transition on a flat plate with a blunt leading edge, Nagarajan, Lele & Ferziger (2007) reported a wavepacket type flow breakdown, which was found to be similar to the varicose type flow breakdown associated with the near-wall inner-mode mechanism (Vaughan & Zaki 2011; Hack & Zaki 2014). In this respect, the results of Nolan & Walsh (2012) may correspond to the inner-mode mechanism of Vaughan & Zaki (2011) and Hack & Zaki (2014), and the results found in the present work are perhaps related to the outer-mode mechanism, because our data reveal a greater number of sinuous instabilities compared with varicose instabilities.

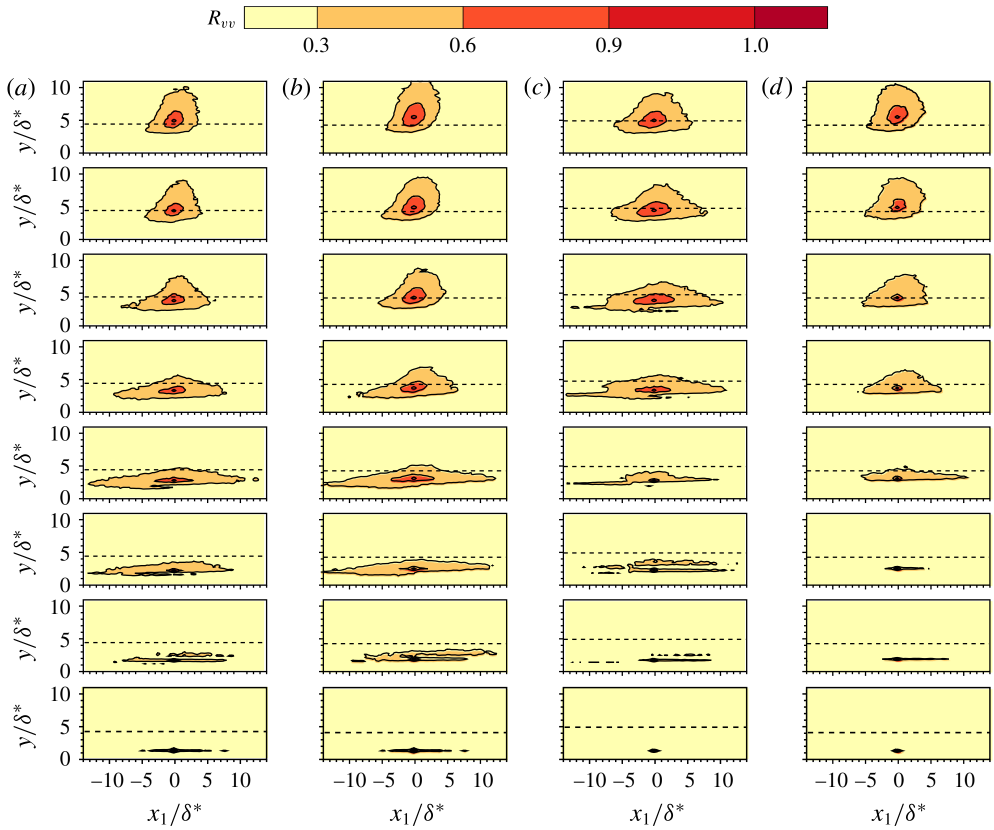

FIGURE 21. (Colour online) (*a*,*b*) Contours of R_{vv} for non-intermittent flows at $z = 14$ mm and $z = -14$ mm for grids A and B respectively at $U_0 = 4.1\ \text{m s}^{-1}$. (*c*,*d*) Contours of R_{vv} for non-intermittent flows at $z = 0$ mm and $z = -14$ mm for grids A and B respectively at $U_0 = 3\ \text{m s}^{-1}$. Contour levels <0.3 are omitted. The dashed line indicates the boundary layer edge.

5.2. *Streak instabilities in the x–z plane*

Time-resolved PIV measurements in the x–z plane at $y = 2.5$ mm were performed for a detailed quantitative assessment of the streak secondary instability characteristics in bypass transition. Using dye-flow visualizations in a water channel, Mans *et al.* (2005) showed the time evolution of the natural unforced sinuous and varicose instabilities in bypass transition. To the best of our knowledge, similar time sequences of quantitative visualizations of these natural unforced instabilities are not available in the experimental literature in bypass transition under a high level of free-stream turbulence. Therefore, time sequences of TR-PIV realizations displaying the evolution of sinuous and varicose instabilities are shown in figures 22 and 23 respectively. Here, the field of view of our measurements was chosen such that the development of these instabilities could be visualized and traced at each instant of time while they propagated in the downstream direction. One may clearly notice that these instabilities are localized and develop on a low-speed streak. The sinuous instability in figure 22 is seen to develop on the low-speed streak located at $z/\delta^* = 8$, whereas the varicose instability in figure 23 develops on the low-speed streak located at $z/\delta^* = 0$. The

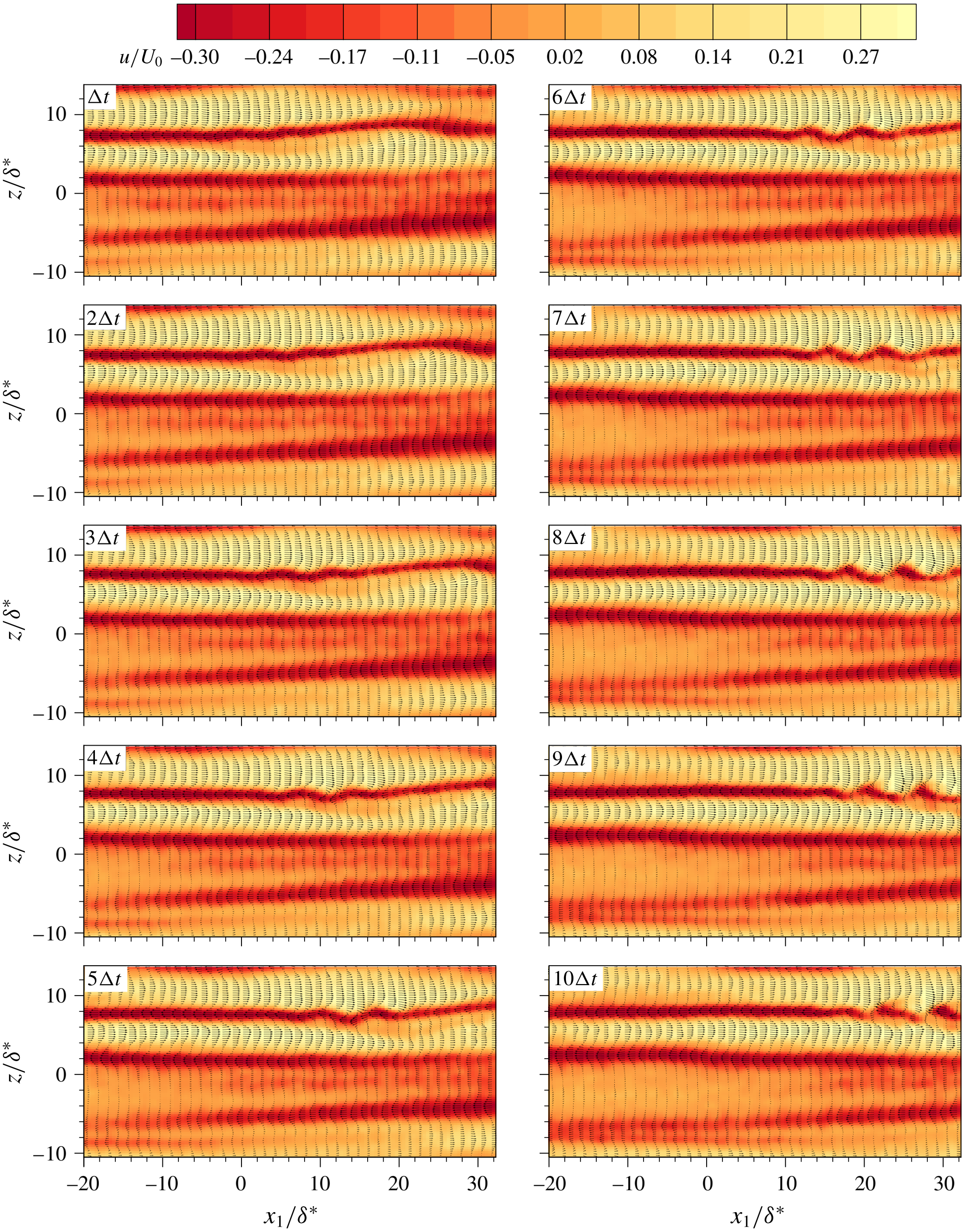

FIGURE 22. (Colour online) Time sequence of a sinuous instability developing on a low-speed streak in the spanwise plane for grid B. The vectors are the fluctuating velocity vectors over the contours of u/U_0. Maintaining the aspect ratio, the region displayed is zoomed in to clearly show the instability development. Each snapshot is separated by $\Delta t = 0.00155$ s.

frequencies of these instabilities in figures 22 and 23 are found to be 281 Hz and 186 Hz respectively.

Furthermore, the varicose instability that originates at the juncture of an incoming high-speed streak and a downstream low-speed streak eventually generates lambda

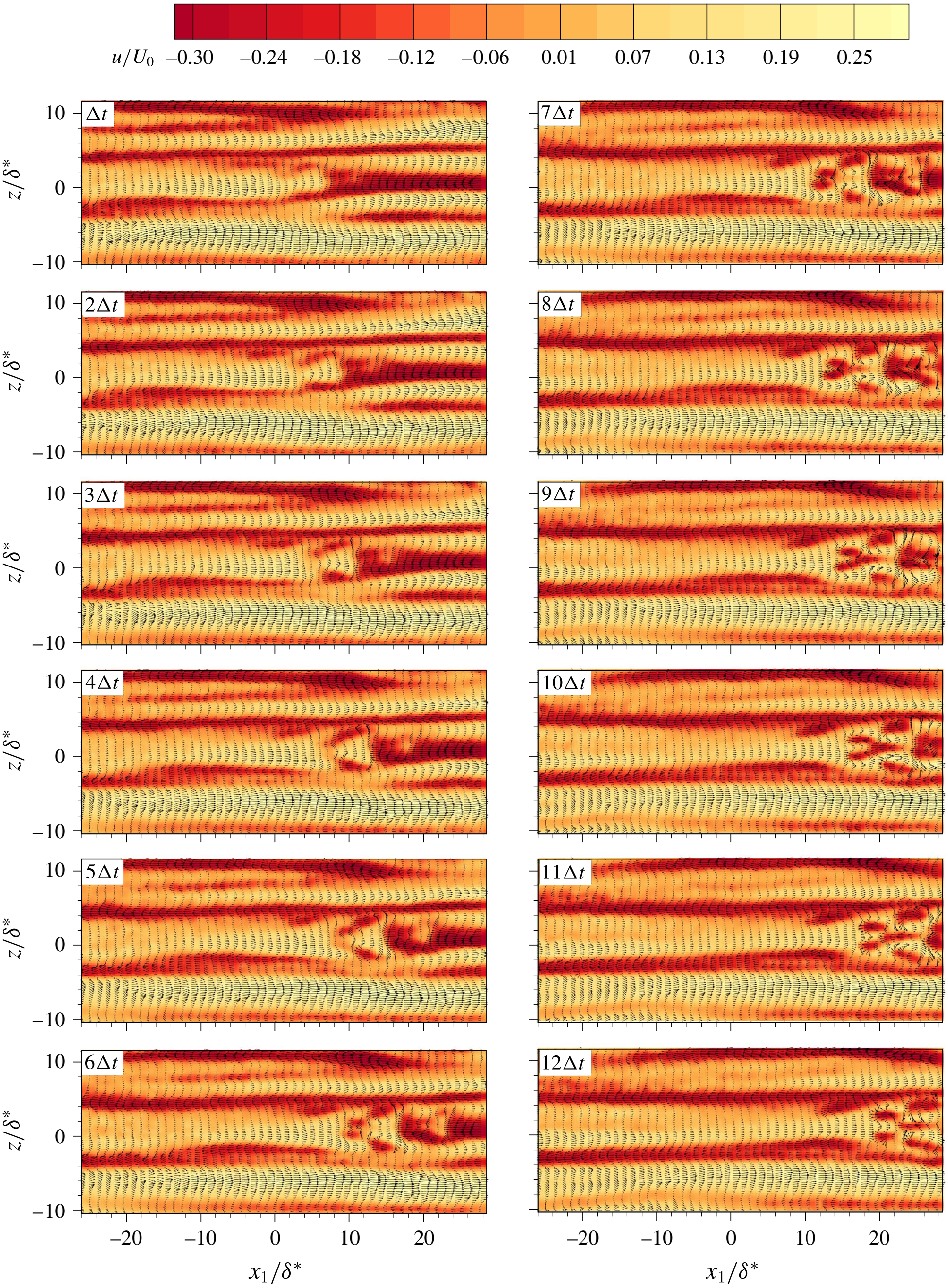

FIGURE 23. (Colour online) Time sequence of a varicose instability developing at the juncture of high- and low-speed streaks in the x–z plane for grid A. The vectors are the fluctuating velocity vectors over the contours of u/U_0. Maintaining the aspect ratio, the region displayed is zoomed in to clearly show the instability development. Each snapshot is separated by $\Delta t = 0.00155$ s.

structures, as can clearly be seen in figure 23. These structures grow in size as time progresses and finally end up with small-scale structures because of their localized inflectional instability, as a lambda structure is generally associated with a highly inflectional velocity profile (e.g. Mandal & Dey 2011). In their DNS of a bypass transition, Brandt *et al.* (2004) also found that the varicose instability is generated due to the interaction of an incoming high-speed streak with a downstream low-speed streak. They further reported that the varicose type instability eventually generates lambda structures, which are susceptible to the localized inflectional instability. Recent DNS on bypass transition by Hack & Zaki (2014) also indicates the presence of lambda structures at the juncture of an incoming high-speed streak and a downstream low-speed streak. The present results, thus, experimentally confirm these numerical observations in bypass transition under an elevated level of free-stream turbulence.

Previous work on bypass transition has indicated that the growth of a sinuous/varicose instability can lead to a turbulent spot in the flow (e.g. Brandt *et al.* 2004; Mans *et al.* 2005; Hack & Zaki 2014). In their experimental work on bypass transition in a water channel, Mans *et al.* (2007) carried out combined PIV and dye visualizations in the spanwise plane, and visualized the flow structures using a moving camera, enabled by a traversing system. Identifying the streak geometry from their measured velocity data, they calculated the secondary amplitude at the centreline of an unstable low-speed streak and estimated the growth rate. They found that the normalized temporal growth rate for the sinuous instability is approximately 0.01; the local boundary layer thickness and the free-stream velocity were used for normalization.

Instead of using the streak geometry to estimate the secondary amplitude and the growth rate, here we follow Lundell (2004) and Hack & Zaki (2014), and utilize a quantitative criterion based on the measured velocity data. We estimate the normalized temporal growth rate as

$$\sigma = \frac{\delta^*}{U_0 \Delta t} \ln \left[\frac{A_s\,(t+\Delta t)}{A_s\,(t)} \right], \tag{5.4}$$

where the secondary amplitude, A_s, similarly to Hack & Zaki (2014), is estimated as $A_s(t) = \max w(x, y = 2.5\ \text{mm}, z, t) - \min w(x, y = 2.5\ \text{mm}, z, t)$. It should be noted that the secondary amplitude in the present work is estimated based on the maximum and minimum spanwise perturbation velocity in the x–z plane located at $y = 2.5$ mm, in the absence of three-dimensional velocity data. Isolating the localized instability region in a PIV realization, we estimate the temporal growth rate of these instabilities. This procedure is illustrated in detail in figure 24. Time-resolved PIV realizations showing the growth of sinuous and varicose instabilities are tracked using a rectangular region at each instant of time, as shown in figures 24(*a*) and 24(*b*) respectively. Then, the secondary amplitude, A_s, is estimated based on the maximum and minimum spanwise perturbation velocity within the rectangular region at that instant of time. Finally, the natural logarithm of the normalized secondary amplitude, $A_s(t+\Delta t)/A_s(t)$, is plotted against the normalized time, $U_0\Delta t/\delta^*$, and the normalized growth rate is estimated from the slope of a straight line fitted to the estimated data, as clearly shown in figures 24(*c*) and 24(*d*) for the sinuous and varicose instabilities respectively. The growth rates, as estimated from figures 24(*c*) and 24(*d*) for the sinuous and varicose instabilities in figures 24(*a*) and 24(*b*), are found to be 0.033 and 0.029 respectively.

However, to find the average growth rates for sinuous and varicose instabilities, several instability events, similar to those in figure 24(*a*,*b*), were identified from

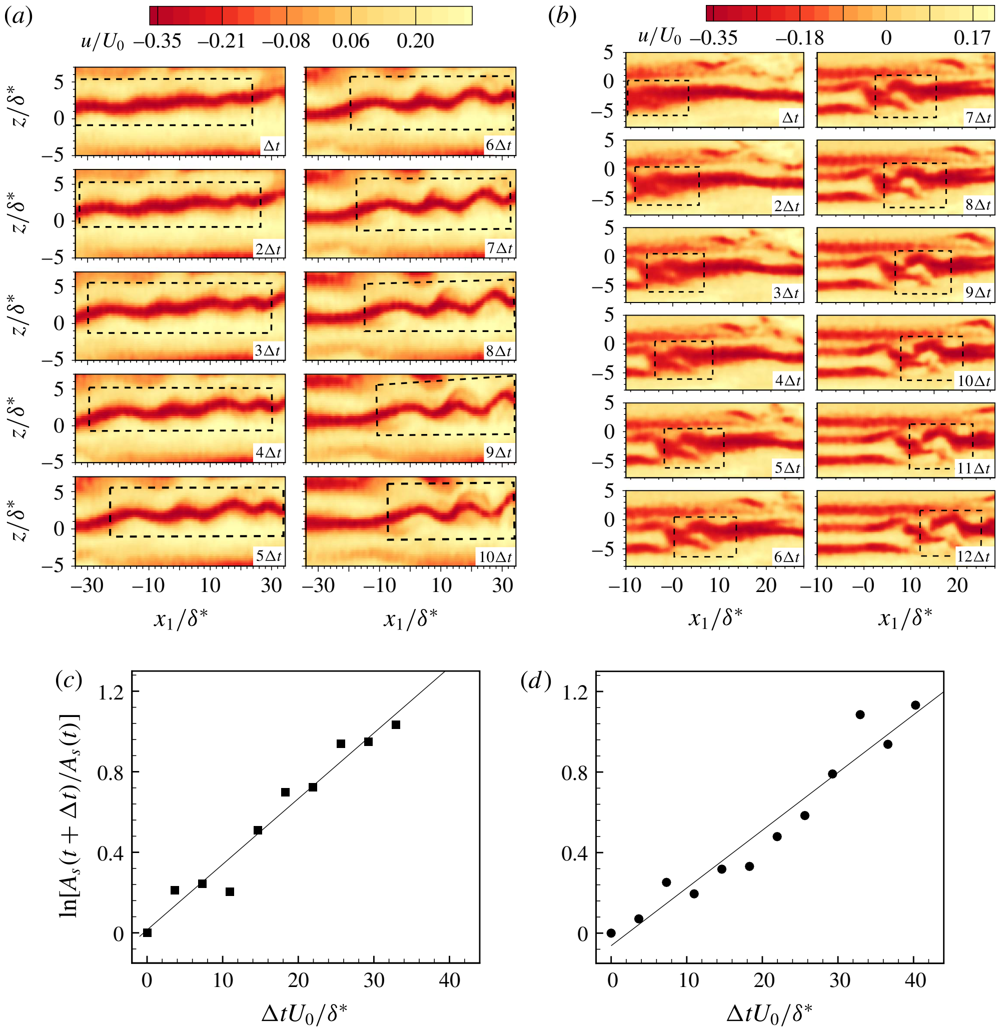

FIGURE 24. (Colour online) Illustration of the procedure to estimate the growth rate for sinuous and varicose instabilities in the *x*–*z* plane. (*a*,*b*) Tracking of sinuous and varicose instability wavepackets at each instant of time to find the secondary amplitude, A_s, for grids B and A respectively. (*c*,*d*) Variation of the normalized secondary amplitude, $A_s(t+\Delta t)/A_s(t)$, with the normalized time, tU_0/δ^*, for the sinuous instability in (*a*) and the varicose instability in (*b*) respectively. Symbols, estimated amplitude; solid line, linear fit.

the entire TR-PIV realizations, and the above procedure was followed to estimate the secondary amplitude for each of these instability events. It should be noted that only those instabilities that grow over a minimum of five time steps are considered for estimating the growth rate. The variation of the normalized secondary amplitude versus the normalized time, for 24 sinuous and 12 varicose instabilities, is shown in figures 25(*a*) and 25(*b*) respectively for grid A. Similarly, figures 25(*c*) and 25(*d*) show the variation of the normalized secondary amplitude versus the normalized time for 24 sinuous and 11 varicose instabilities respectively for grid B. The scatter in the data as seen in these figures was found to be similar to that found by Mans *et al.* (2007).

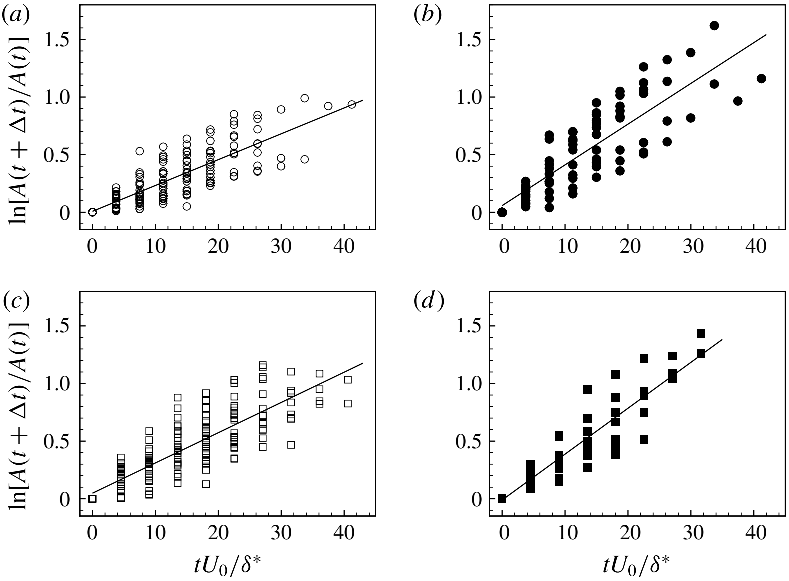

FIGURE 25. Average growth rates of sinuous and varicose instabilities based on several observations. (*a*) Sinuous instability for grid A. (*b*) Varicose instability for grid A. (*c*) Sinuous instability for grid B. (*d*) Varicose instability for grid B. Symbols, estimated amplitude; solid line, linear fit to the data.

However, an average growth rate for the sinuous/varicose instability for a particular grid was estimated based on a straight line fit to all of the data for a particular case (i.e. sinuous/varicose). The sinuous growth rates for grids A and B were found to be 0.022 and 0.025 respectively, whereas the varicose growth rates for grids A and B were found to be 0.035 and 0.04 respectively.

The present growth rate for the sinuous instability is comparable with the theoretical growth rates reported by Andersson *et al.* (2001) and Schlatter *et al.* (2008). Hack & Zaki (2014) reported the normalized growth rate based on the length and velocity scales corresponding to their inlet Reynolds number, $Re = 800$. Therefore, to compare our present data with their calculated growth rates, we estimate the equivalent length scale at that Reynolds number based on our present free-stream velocity and kinematic viscosity. According to this equivalent length scale and the free-stream velocity, the present growth rates for the sinuous instability are found to be 0.02 and 0.022 for grids A and B respectively, whereas the growth rates for the varicose instability are found to be 0.031 and 0.035 for grids A and B respectively. Therefore, the present growth rate for the sinuous instability is found to be within the range reported by Hack & Zaki (2014). The present growth rate for the varicose instability is also found to be comparable with their growth rate statistics for the inner mode.

Figure 26 shows the histograms of the convection velocity and the wavelength for both sinuous and varicose instabilities; here, white bars refer to the sinuous instability and black bars refer to the varicose instability. It should be noted that these statistics are based on all of the sinuous and varicose instabilities identified for both of the grids. Following a similar methodology to that in § 5.1.1, the propagation/convection velocity is estimated from the space–time shift of these instabilities, and the wavenumbers are estimated from the measured wavelengths. However, we may mention that in

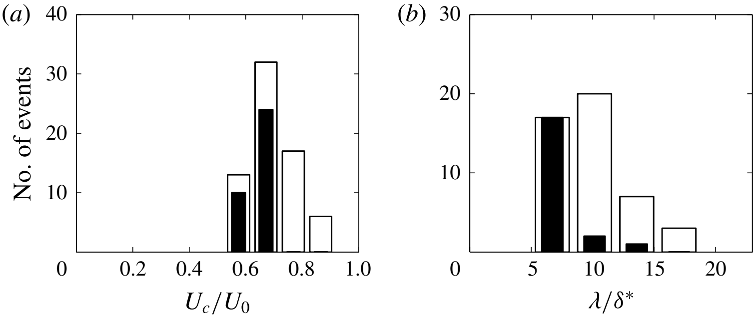

FIGURE 26. Histograms of the convection velocity (*a*) and the wavenumber (*b*) for the sinuous and varicose instabilities. White bars, sinuous instability; black bars, varicose instability.

contrast to the oscillations in the x–y plane, which were visualized using the $\omega_z\delta^*/U_0$ contours, wavy oscillations (sinuous/varicose) in the x–z plane are visualized using the u/U_0 contours to estimate the wavelength and convection velocity reported in this section. Figure 26(*a*) shows that the convection velocity of the sinuous instability varies from $0.5U_0$ to $0.9U_0$ with a peak at approximately $0.7U_0$, and that of the varicose instability varies approximately from $0.5U_0$ to $0.7U_0$ with a peak at approximately $0.7U_0$. However, the average convection velocities for the sinuous and varicose instabilities are found to be $0.70U_0$ and $0.64U_0$ respectively. These results are comparable to the numerical simulations of Brandt *et al.* (2004) and Hack & Zaki (2014). Based on their dye-flow visualizations at two different wall-normal heights in a water channel, Mans *et al.* (2005) reported a value of $0.75U_0$ for a single sinuous instability and $0.47U_0$ for a single varicose instability. The convection velocities estimated from the present TR-PIV measurements are thus comparable with their visualization results. Similarly, figure 26(*b*) shows that the normalized wavelength varies from 5 to 19 for the sinuous instability and from 5 to 14 for the varicose instability. These values are also found to be consistent with the simulated values reported in the literature (e.g. Brandt *et al.* 2004; Schlatter *et al.* 2008; Hack & Zaki 2014). Considering three sinuous instabilities, a similar variation in wavelength was also reported by Mans *et al.* (2007) based on their PIV measurements in a water channel flow. One may also notice that the estimated and calculated values of the convection velocity and the wavelength of the oscillating shear layers in the x–y plane (figure 23) are found to be within the range seen in figure 26.

6. Streak amplitude

Amplification of sinuous and varicose instabilities, as discussed in § 5.2, is often attributed to the streak amplitude, usually defined based on the velocity difference between a low-speed streak and a high-speed streak (e.g. Andersson *et al.* 2001) or based on the maximum absolute value of the perturbation velocity (Vaughan & Zaki 2011). Although various experimental works have been carried out in bypass transition under an elevated level of free-stream turbulence, the streak amplitude in terms of the velocity difference, and its relation to streak secondary instability have not been experimentally investigated and reported to the best of our knowledge. Therefore, we estimated the streak amplitude using wide field of view conventional PIV measurements in the x–z plane. The measurements were carried out at the same

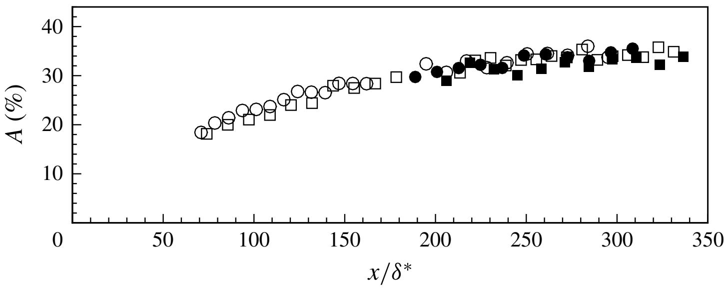

FIGURE 27. Variation of the streak amplitude with the streamwise distance for grids A and B. Symbols: circle, grid A; square, grid B; the open and filled symbols denote the data measured in the x–z planes located at $y = 1.5$ mm and 2.5 mm respectively.

free-stream velocities as given in table 4. Following Andersson *et al.* (2001), the streak amplitude is defined here as

$$A(x) = \frac{1}{2U_0}\left[\max_{z,N}(U_I - U_B) - \min_{z,N}(U_I - U_B)\right], \tag{6.1}$$

where U_B is the Blasius velocity and N is the number of PIV realizations. To cover a large streamwise extent, the PIV measurements were carried out in two separate fields of view centred at $x = 300$ mm and 600 mm respectively, as stated in § 2.2. Our measurements in the first and second fields of view extended from $x = 164$ mm to 436 mm and $x = 446$ mm to 754 mm respectively. The measurement plane was located at $y = 1.5$ mm for both of these fields of view. However, to investigate the amplitude variation with respect to the wall-normal distance, the PIV measurements in the second field of view were also carried out at $y = 2.5$ mm. We may also mention that the wall-normal locations, $y = 1.5$ mm and $y = 2.5$ mm, closely correspond to the locations of the peak u_{rms} values in their wall-normal distributions at $x = 300$ mm and 600 mm respectively.

Figure 27 shows the variation of the estimated streak amplitude, A, in the downstream direction for both grid A and grid B. The open and filled symbols in figure 27 refer to the data measured at $y = 1.5$ mm and 2.5 mm respectively. The streak amplitude, A, was estimated utilizing a minimum of 990 PIV realizations for each case considered. The data in figure 27 show that the streak amplitude increases in the downstream direction and saturates at a value of approximately 35 % of the free-stream velocity for both of the grids. We also notice that the data measured at two different x–z planes do not show significant differences in the estimated streak amplitudes.

Although the streak amplitude at the end of the first field of view was found to be approximately 29 % of the free-stream velocity (figure 27), the hotwire signals at that location were not found to be intermittent for either of the grids. Similarly, the spatial PIV data in the first field of view revealed no sign of sinuous and varicose instabilities for either of the grids. The typical streaky structures, which were seen in the first field of view, are illustrated in figure 28(a) for grid A. On the other hand, the flow in the second field of view was found to be intermittent starting at approximately $x/\delta^* \approx 210$, and the flow intermittency at the centre of the second field of view was found to be 1.5 % and 2 % for grids A and B respectively. A signature of the streak secondary instability in the second field of view can also be noticed in

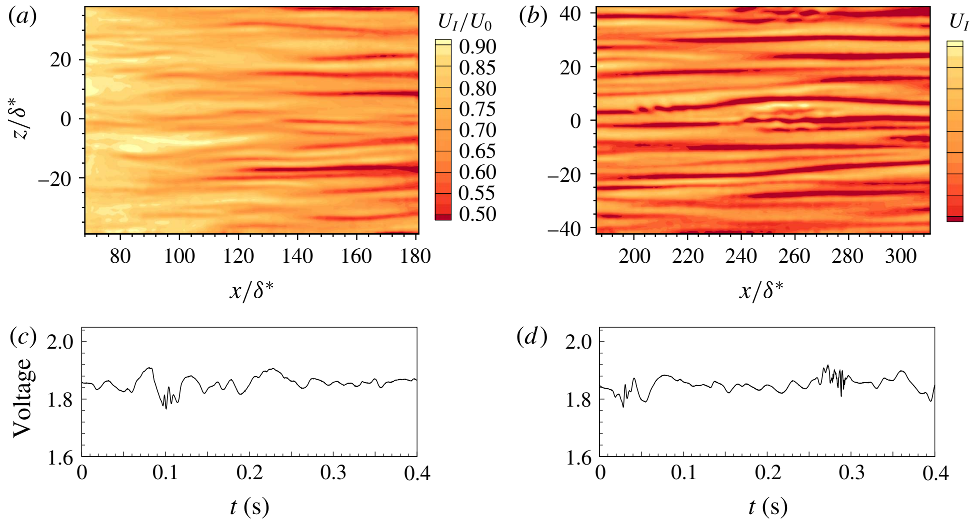

FIGURE 28. (Colour online) (*a*,*b*) Instantaneous PIV realizations in the first and second fields of view depicting typical streaky structures measured at $y=1.5$ mm and 2.5 mm respectively for grid A. (*c*,*d*) Typical hotwire signals at $x/\delta^*=210$, $z/\delta^*=0$ and $x/\delta^*=250$, $z/\delta^*=0$ respectively for grid A. The wall-normal location of the hotwire was at $y=2.5$ mm.

the instantaneous PIV realizations, as illustrated in figure 28(*b*) for grid A. One of these instability packets in this figure can clearly be seen at approximately $x/\delta^*=200$ and $z/\delta^*=5$, where the streak amplitude is found to be approximately 30 %. The typical hotwire signals in the plate centreline at $x/\delta^*=210$ and 250, as shown in figures 28(*c*) and 28(*d*) respectively, also indicate a sign of some flow instability for grid A. The value of the streak amplitude over the streamwise extent where the instabilities, as shown in figures 22 and 23, were measured was found to be above 30 % of the free-stream velocity. Therefore, the present measurements indicate that the streak secondary instability may set in at a streak amplitude of approximately 30 % of the free-stream velocity.

The present threshold amplitude, 30 %, is slightly higher than the value of Andersson *et al.* (2001), who reported the threshold value to be 26 % of the free-stream velocity. It is also higher than the threshold value of Hack & Zaki (2014), who reported that a streak amplitude of 20 %–35 % of the free-stream velocity can lead to a positive growth rate for an outer instability. Although the present measured value is well within the bounds reported by these authors, the 4 %–10 % difference compared with the values reported by these authors may be due to the following reason. In an experiment, the visualization of an instability wavepacket may be prominent in the velocity contours only when its amplification is large enough, although its amplification may start earlier than its manifestation in the velocity contours. Hack & Zaki (2014) reported a similar observation in the numerical simulation of bypass transition.

7. Summary and concluding remarks

Localized secondary instability events in bypass boundary layer transition have been experimentally investigated using three different PIV configurations. The conventional

PIV measurements in the x–y plane clearly revealed that the present mean flow data are consistent with those in the published literature (see figure 6).

A simultaneous orthogonal dual-plane PIV technique was utilized to acquire simultaneous PIV data in the x–y and x–z planes. These measurements indicated that the origin of an inclined shear layer in the x–y plane can be attributed to the spanwise meandering motions of low- and high-speed streaks (see figure 9). Moreover, the present simultaneous measurements, for the first time, experimentally facilitate the quantitative x–y plane visualization of streaky structures undergoing sinuous/varicose motion in the x–z plane in bypass transition under an elevated level of free-stream turbulence. The sinuous and varicose streak instabilities in the x–z plane were found to be associated with oscillating shear layers in the x–y plane. The shear layer oscillation corresponding to a varicose instability was found to occur closer to the wall compared with the oscillation corresponding to a sinuous instability (see figure 10 for example). Although the sinuous and varicose instabilities in the x–z plane were always found to be associated with oscillating shear layers in the x–y plane, the converse may not be true, as some simultaneous PIV realizations revealed that while there exist significant shear layer oscillations in the x–y plane near the boundary layer edge, the corresponding near-wall streaks in the x–z plane do not show any appreciable varicose/sinuous motion (see figure 12*a*,*b*). This indicates that an instability wavepacket can originate near the boundary layer edge.

Time-resolved PIV measurements in the x–y plane were carried out to investigate the time evolution of the oscillating shear layers. The data show that an oscillation may develop at either the leading edge or the trailing edge portion of a lifted-up inclined shear layer, and these shear layer oscillations, while comparing with the simultaneous PIV data, are found to be similar to those that correspond to sinuous and varicose motions in the x–z plane respectively. Interestingly, the one-dimensional linear stability analysis on the realistic base velocity profile of a low-speed steak undergoing shear layer oscillation in the x–y plane indicates that an oscillation in an inclined shear layer develops due to the linear instability, as the estimated wavelength and the frequency of oscillation are found to be comparable to the calculated ones (see figure 19). Moreover, the phase velocity associated with an inclined shear layer far away from the wall is higher than the phase velocity associated with an inclined shear layer closer to the wall. This is consistent with the recent theoretical and numerical findings of Vaughan & Zaki (2011) and Hack & Zaki (2014). In addition, the role of free-stream turbulence in inception of these instabilities was examined using the correlation contours of the wall-normal fluctuating velocity, which indicated the existence of a clear relation between the free-stream turbulence and the boundary layer streaks (figures 20 and21).

Therefore, the simultaneous PIV measurements in the x–y and x–z planes and the TR-PIV measurements in the x–y plane collectively corroborated the fact that an instability wavepacket on a low-speed streak can get excited near the boundary layer edge (see figures 12 and 14 for example). Hence, these measurements provide experimental support to the proposal that a secondary instability wavepacket can originate near the boundary layer edge (e.g. Jacobs & Durbin 2001; Durbin & Wu 2007; Schlatter *et al.* 2008; Hack & Zaki 2014). Further, our measurements clearly show that a sinuous instability in its nonlinear saturated stage can lead to an incipient turbulent spot with significant detached vorticity and counter-rotating vortex pairs (see figures 11, 14 and 15). The existence of such a scenario for a varicose instability may also be deduced from the presented data (see figure 10*d* for example).

The TR-PIV measurements in the x–z plane enabled us to visualize the quantitative time sequences of the localized sinuous and varicose instabilities. The present measurements confirm the numerical observations of Brandt *et al.* (2004) and Hack & Zaki (2014) that a varicose instability can occur due to the interaction of an incoming high-speed streak with a downstream low-speed streak, leading to an eventual generation of lambda structures (see figure 23). To the best of our knowledge, this experimental observation is reported for the first time in bypass transition at an elevated level of free-stream turbulence, substantiating the need for a TR-PIV measurement in bypass transition studies. However, the present measurements also show that other than the juncture of a high-speed and a low-speed streak, a varicose instability may even develop in the middle of a low-speed streak (see figures 10*c* and 12*c*for example).

The TR-PIV data were also utilized to estimate the growth rate of sinuous and varicose instabilities in the x–z plane. The statistical analysis shows that the growth rate of the sinuous instability is lower compared with the varicose instability. However, the growth rates of these instabilities are found to be consistent with the theoretical values reported in the literature (e.g. Andersson *et al.* 2001; Schlatter *et al.* 2008; Hack & Zaki 2014). Similarly, the statistics of the estimated convection velocity and wavelength are found to compare well with the previous numerical and theoretical data. The value of the streak amplitude, at the streamwise location where the sign of streak secondary instability becomes evident in the velocity contours, is found to be $\sim$30 % of the free-stream velocity. This value is found to be within the bounds reported by Andersson *et al.* (2001) and Hack & Zaki (2014).

In conclusion, the present work on bypass transition provides experimental evidence of the fact that the boundary layer edge can be a receptive site for excitation of a localized secondary instability wavepacket besides other excitation sites, such as the juncture between a low-speed streak and a high-speed streak. The effect of free-stream turbulence in the excitation of a secondary instability wavepacket which is manifested initially as an oscillation of a lifted-up shear layer at the boundary layer edge cannot be ruled out. Moreover, the natural secondary instability characteristics in bypass transition for parallel and square grids are found to be similar for nearly the same free-stream turbulent characteristics.

Acknowledgements

Financial support from IIT Kanpur for the PIV systems through CARE and initiation grants is gratefully acknowledged. In this regard, we are grateful to Professors A. Kushari, D. Das, K. Poddar, S. K. Mishra, V. Shankar, M. K. Das and A. K. Saha for their help and support. Financial support from AR and DB is also gratefully acknowledged. We are grateful to Professors D. Das and S. Mittal for providing their high-quality CCD cameras, and Professor K. Poddar for lending us his laser unit. Comments and suggestions on the initial draft of this paper by Professor J. Dey are gratefully acknowledged. We are grateful to Professor B. Ganapathisubramani for helpful discussions on simultaneous PIV measurements over email. We also thank Mr V. Dabaria for the linear stability code and Mr Y. Arafath, Mr K. K. Bharadwaj, Dr C. L. Dora and Dr J. N. Murugan for their experimental help and fruitful discussion.

REFERENCES

ALKISLAR, M. B., KROTHAPALLI, A. & LOURENCO, L. M. 2003 Structure of a screeching rectangular jet: a stereoscopic particle image velocimetry study. *J. Fluid Mech.* **489**, 121–154.

ANDERSSON, P., BERGGREN, M. & HENNINGSON, D. S. 1999 Optimal disturbances and bypass transition in boundary layers. *Phys. Fluids* **11**, 134–150.

ANDERSSON, P., BRANDT, L., BOTTARO, A. & HENNINGSON, D. S. 2001 On the breakdown of boundary layer streaks. *J. Fluid Mech.* **428**, 29–60.

ARNAL, D. & JUILLEN, J. C. 1978 Contribution experimentale à l'ètude de la receptivité d'une couche limite laminarire, à la turbulence de l'ecoulement general. *Rap. Tech.* 1/5018 AYD ONERA.

ASAI, M., MINAGAWA, M. & NISHIOKA, M. 2002 The instability and breakdown of a near-wall low-speed streak. *J. Fluid Mech.* **455**, 289–314.

BALAMURUGAN, G. 2014 Experiments on bypass boundary layer transition using parallel rod grids. Master's thesis, Indian Institute of Technology, Kanpur, India.

BATCHELOR, G. K. 1982 *The Theory of Homogeneous Turbulence*. Cambridge University Press.

BOUTILIER, M. S. H. & YARUSEVYCH, S. 2012 Separated shear layer transition over an airfoil at a low Reynolds number. *Phys. Fluids* **24**, 084105,1–23.

BRANDT, L. 2007 Numerical studies of the instability and breakdown of a boundary-layer low-speed streak. *Eur. J. Mech. (*B*/Fluids)* **26**, 64–82.

BRANDT, L., SCHLATTER, P. & HENNINGSON, D. S. 2004 Transition in boundary layers subject to free-stream turbulence. *J. Fluid Mech.* **517**, 167–198.

CHERNORAY, V. G., KOZLOV, V. V., LOFDAHL, L. & CHUN, H. H. 2006 Visualization of sinusoidal and varicose instabilities of streaks in a boundary layer. *J. Vis.* **9**, 437–444.

COLEMAN, H. W. & STEELE, W. G. 2009 *Experimentation, Validation, and Uncertainty Analysis for Engineers*. Wiley.

DABARIA, V. 2015 Linear stability analysis of measured inflectional velocity profiles in separated boundary layer flows. Master's thesis, Indian Institute of Technology, Kanpur, India.

DENNIS, D. J. C. & NICKELS, T. B. 2011 Experimental measurement of large-scale three-dimensional structures in a turbulent boundary layer. Part 1. Vortex packets. *J. Fluid Mech.* **673**, 180–217.

DURBIN, P. & WU, X. 2007 Transition beneath vortical disturbances. *Annu. Rev. Fluid Mech.* **39**, 107–128.

ELLINGSEN, T. & PALM, E. 1975 Stability of linear flow. *Phys. Fluids* **18**, 487–488.

FRANSSON, J. H. M., MATSUBARA, M. & ALFREDSSON, P. H. 2005 Transition induced by freestream turbulence. *J. Fluid Mech.* **527**, 1–25.

GANAPATHISUBRAMANI, B., LONGMIRE, E. K., MARUSIC, I. & POTHOS, S. 2005 Dual-plane PIV technique to determine the complete velocity gradient tensor in a turbulent boundary layer. *Exp. Fluids* **39**, 222–231.

GOLDSTEIN, M. E. & WUNDROW, D. W. 1998 On the environmental realizability of algebraically growing disturbances and their relation to Klebanoff modes. *Theor. Comput. Fluid Dyn.* **10**, 171–186.

GOMES-FERNANDES, R., GANAPATHISUBRAMANI, B. & VASSILICOS, J. C. 2012 Particle image velocimetry study of fractal-generated turbulence. *J. Fluid Mech.* **711**, 306–336.

HACK, M. J. P. & ZAKI, T. A. 2014 Streak instabilities in boundary layers beneath free-stream turbulence. *J. Fluid Mech.* **741**, 280–315.

HAMBLETON, W. T., HUTCHINS, N. & MARUSIC, I. 2006 Simultaneous orthogonal-plane particle image velocimetry measurements in a turbulent boundary layer. *J. Fluid Mech.* **560**, 53–64.

HANSON, R. E., BUCKLEY, H. P. & LAVOIE, P. 2012 Aerodynamic optimization of the flat-plate leading edge for experimental studies of laminar and transitional boundary layers. *Exp. Fluids* **53**, 863–871.

HERNON, D., WALSH, E. J. & MCELIGOT, D. M. 2007 Experimental investigation into the routes to bypass transition and the shear-sheltering phenomenon. *J. Fluid Mech.* **591**, 461–479.

HULTGREN, L. S. & GUSTAVSSON, L. H. 1981 Algebraic growth of disturbances in a laminar boundary layer. *Phys. Fluids* **24**, 1000–1004.

JACOBS, R. G. & DURBIN, P. A. 2001 Simulations of bypass transition. *J. Fluid Mech.* **428**, 185–212.

KACHANOV, Y. S. 1994 Physical mechanism of laminar-boundary-layer transition. *Annu. Rev. Fluid Mech.* **26**, 411–482.

KÄHLER, C. J. & KOMPENHANS, J. 2000 Fundamentals of multiple plane stereo particle image velocimetry. *Exp. Fluids* **29**, S070–S077.

Kendall, J. M. 1985 Experimental study of disturbances produced in a pre-transitional laminar boundary layer by weak freestream turbulence. *AIAA Paper* 85-1695.

Kendall, J. M. 1998 Experiments on boundary layer receptivity to freestream turbulence. *AIAA Paper* 98-0530.

King, R. A. 2000 Receptivity and growth of two- and three-dimensional disturbances in a Blasius boundary layer. PhD thesis, Massachusetts Institute of Technology, Cambridge, MA.

Klebanoff, P. S. 1971 Effect of freestream turbulence on the laminar boundary layer. *Bull. Am. Phys. Soc.* **10**, 1323–1334.

Klingmann, R. G. B., Boiko, A. V., Westin, K. J. A., Kozlov, V. V. & Alfredsson, P. H. 1993 Experiments on the stability of Tollmien–Schichting waves. *Eur. J. Mech.* (B*/Fluids)* **12**, 493–514.

Konishi, Y. & Asai, M. 2010 Development of subharmonic disturbance in spanwise-periodic low-speed streaks. *Fluid Dyn. Res.* **42**, 035504.

Kuan, C. L. & Wang, T. 1990 Investigation of the intermittent behavior of transitional boundary layer using a conditional averaging technique. *Exp. Therm. Fluid Sci.* **3**, 157–173.

Kurian, T. & Fransson, J. H. M. 2009 Grid-generated turbulence revisited. *Fluid Dyn. Res.* **41**, 021403.

Landahl, M. T. 1980 A note on an algebraic instability of inviscid parallel shear flows. *J. Fluid Mech.* **98**, 243–251.

Lazar, E., DeBlauw, B., Glumac, N., Dutton, C. & Elliott, G. 2010 A practical approach to PIV uncertainty analysis. *AIAA Paper* 2010-4355.

Leib, S. J., Wundrow, D. W. & Goldstein, M. E. 1999 Effect of free-stream turbulence and other vortical disturbances on a laminar boundary layer. *J. Fluid Mech.* **380**, 169–203.

Li, Y. & Gaster, M. 2006 Active control of boundary-layer instabilities. *J. Fluid Mech.* **550**, 185–205.

Liu, Z., Adrian, R. J. & Hanratty, T. J. 2001 Large-scale modes of turbulent channel flow: transport and structure. *J. Fluid Mech.* **448**, 53–80.

Lourenco, L. M. & Krothapalli, A. 2000 TRUE resolution PIV: a mesh-free second order accurate algorithm. In *Proceedings of the International Conference in Applications of Lasers to Fluid Mechanics, Lisbon, Portugal*.

Luchini, P. 2000 Reynolds-number-independent instability of the boundary layer over a flat surface: optimal perturbations. *J. Fluid Mech.* **404**, 289–309.

Lundell, F. 2004 Streak oscillations of finite length: disturbance evolution and growth. *Phys. Fluids* **16**, 3227–3230.

Mandal, A. C. & Dey, J. 2011 An experimental study of boundary layer transition induced by a cylinder wake. *J. Fluid Mech.* **684**, 60–84.

Mandal, A. C., Venkatakrishnan, L. & Dey, J. 2010 A study on boundary layer transition induced by freestream turbulence. *J. Fluid Mech.* **660**, 114–146.

Mans, J., Kadijk, E. C., de Lange, H. C. & van Steenhoven, A. A. 2005 Breakdown in a boundary layer exposed to free-stream turbulence. *Exp. Fluids* **39**, 1071–1083.

Mans, J., de Lange, H. C. & van Steenhoven, A. A. 2007 Sinuous breakdown in a flat plate boundary layer exposed to free-stream turbulence. *Phys. Fluids* **19**, 088101.

Matsubara, M. & Alfredsson, P. H. 2001 Disturbance growth in boundary layers subjected to free-stream turbulence. *J. Fluid Mech.* **430**, 149–169.

Morkovin, M. V. 1969 The many faces of transition. In *Viscous Drag Reduction* (ed. C. S. Wells), Plenum.

Nagarajan, S., Lele, S. K. & Ferziger, J. H. 2007 Leading-edge effects in bypass transition. *J. Fluid Mech.* **572**, 471–504.

Nishioka, M., Asai, M. & Iida, S. 1981 Wall phenomena in the final stage of transition to turbulence. In *Transition and Turbulence* (ed. R. E. Meyer), pp. 113–126. Academic.

Nolan, K. P. & Walsh, E. J. 2012 Particle image velocimetry measurements of a transitional boundary layer under free stream turbulence. *J. Fluid Mech.* **702**, 215–238.

NOLAN, K. P., WALSH, E. J. & MCELIGOT, D. M. 2010 Quadrant analysis of a transitional boundary layer subject to free-stream turbulence. *J. Fluid Mech.* **658**, 310–335.

O'NEILL, P. L., NICOLAIDES, D., HONNERY, D. & SORIA, J. 2004 Autocorrelation functions and the determination of integral length with reference to experimental and numerical data. In *15th Australasian Fluid Mechanics Conference, The University of Sydney, Sydney, Australia*, pp. 13–17.

OVCHINNIKOV, V., CHOUDHARI, M. M. & PIOMELLI, U. 2008 Numerical simulations of boundary-layer bypass transition due to high-amplitude free-stream turbulence. *J. Fluid Mech.* **613**, 135–169.

PASQUALE, D. D. & RONA, A. 2010 Data assessment of two ERCOFTAC transition test cases for CFD validation. In *Proceedings of the 7th International Conference on Heat Transfer, Fluid Mechanics and Thermodynamics, Turkey 19–21 July*, pp. 2155–2160.

PHANI KUMAR, P., MANDAL, A. C. & DEY, J. 2015 Effect of a mesh on boundary layer transitions induced by free-stream turbulence and an isolated roughness element. *J. Fluid Mech.* **772**, 445–477.

PHILIP, J., KARP, M. & COHEN, J. 2016 Streak instability and generation of hairpin-vortices by a slotted jet in channel crossflow: experiments and linear stability analysis. *Phys. Fluids* **28**, 014103,1–21.

POOK, D. A. & WATMUFF, J. H. 2014 Streak generation in wind tunnels. *Phys. Fluids* **26**, 073605.

POOK, D. A., WATMUFF, J. H. & ORIFICI, A. C. 2016 Test section streaks originating from imperfections in a zither located upstream of a contraction. *J. Fluid Mech.* **787**, 254–291.

RAFFEL, M., WILLERT, C. E., WERELEY, S. & KOMPENHANSÜRGEN, J. 2013 *Particle Image Velocimetry: A Practical Guide*. Springer.

RAGHAV, V. & KOMERATH, N. 2014 Velocity measurements on a retreating blade in dynamic stall. *Exp. Fluids* **55**, 1669.

RAI, M. M. & MOIN, P. 1993 Direct numerical simulation of transition and turbulence in a spatially evolving boundary layer. *J. Comput. Phys.* **109**, 169–192.

REED, H. L., SARIC, W. S. & ARNAL, D. 1996 Linear stability theory applied to boundary layers. *Annu. Rev. Fluid Mech.* **28**, 389–428.

REUTER, J. & REMPFER, D. 2004 Analysis of pipe flow transition. Part I. Direct numerical simulation. *Theor. Comput. Fluid Dyn.* **17**, 273–292.

RIST, U. & FASEL, H. 1995 Direct numerical simulation of controlled transition in a flat-plate boundary layer. *J. Fluid Mech.* **298**, 211–248.

ROACH, P. E. 1987 The generation of nearly isotropic turbulence by means of grids. *Intl J. Heat Fluid Flow* **8**, 82–92.

ROACH, P. E. & BRIERLY, D. H. 1992 The influence of a turbulent freestream on zero pressure gradient transitional boundary layer development, part I: test cases T3A and T3B. In *ERCOFTAC Workshop: Numerical Simulation of Unsteady Flows and Transition to Turbulence, Lausanne*, pp. 319–347. Cambridge University Press.

SARIC, W. S., REED, H. L. & KERSCHEN, E. J. 2002 Boundary-layer receptivity to freestream disturbances. *Annu. Rev. Fluid Mech.* **34**, 291–319.

SCHLATTER, P., BRANDT, L., DE LANGE, H. C. & HENNINGSON, D. S. 2008 On streak breakdown in bypass transition. *Phys. Fluids* **20**, 101505.

SCHMID, P. J. & HENNINGSON, D. S. 2001 *Stability and Transition in Shear Flows*. Springer.

SINGER, B. A. 1996 Characteristics of a young turbulent spot. *Phys. Fluids* **8**, 509–521.

VAUGHAN, N. J. & ZAKI, T. A. 2011 Stability of zero-pressure-gradient boundary layer distorted by unsteady Klebanoff streaks. *J. Fluid Mech.* **681**, 116–153.

WATMUFF, J. H. 2006 Effects of weak free stream nonuniformity on boundary layer transition. *Trans. ASME J. Fluids Engng* **128**, 247–257.

WESTIN, K. J. A., BOIKO, A. V., KLINGMANN, B. G. G., KOZLOV, V. V. & ALFREDSSON, P. H. 1994 Experiments in a boundary layer subjected to free stream turbulence. Part 1. Boundary layer structure and receptivity. *J. Fluid Mech.* **281**, 193–218.

YAVUZKURT, S. 1984 A guide to uncertainty analysis of hot-wire data. *Trans. ASME J. Fluids Engng* **106**, 181–186.

ZAKI, T. A. & DURBIN, P. A. 2005 Mode interaction and the bypass route to transition. *J. Fluid Mech.* **531**, 85–111.

ZAKI, T. A. & SAHA, S. 2009 On shear sheltering and the structure of vortical modes in single- and two-fluid boundary layers. *J. Fluid Mech.* **626**, 111–147.